Nanophotonic Assemblies and Light Management for Increased Absorption and Photoluminescence

A THESIS
SUBMITTED TO THE FACULTY OF THE
UNIVERSITY OF MINNESOTA
BY

MATTHEW KWOKMAN QUAN

IN PARTIAL FULFILLMENT OF THE REQUIREMENTS
FOR THE DEGREE OF
MASTERS OF SCIENCE

Vivian E. Ferry, Advisor

October, 2020

Acknowledgements

During my time at the University of Minnesota I have been fortunate to receive support and guidance from a number of faculty, staff, and students. I am grateful for the opportunity that Minnesota has provided to work with and learn from these exceptional people.

First, I would like to thank my adviser Vivian Ferry. Her drive to ask interesting scientific questions to push the boundaries of science showed me what it takes to be an effective scientist. I am also thankful for the support and guidance from collaborators Dave Flannigan at the Minnesota and Nobuhiro Yanai at Kyushu University. I would also like to thank Dave Flannigan and Renee Frontiera for their guidance as committee members for my master's thesis defense.

It has been rewarding to work with an outstanding group of students in my graduate career. I would like to thank Ryan Gnabasik for his astute insight in the data analysis of ultrafast electron microscopy measurements. I would also like to thank Rena Haruki for her help creating the upconverting hydrogel and guiding me around Kyushu during my time in Japan. In the Ferry group, I would like to thank Ryan Connell for his assistance in understanding how to efficiently and effectively run Monte Carlo and Finite Difference Time Domain simulations as well as monthly trips to taste the new burger of the month. I would like to thank Dana Dement for her work in developing the direct write electron beam lithography method to create patterned quantum dot solids and ellipsometry modeling. I would also like to thank Mayank Puri for his help with ligand exchange methods and other wet lab chemistry techniques along with the weekly tea breaks we had to chat and decompress from the busy research life. I have also been fortunate to work with and mentor a promising undergraduate researcher in Sihoon Moon who investigated the aggregation of APTES due to hydrolysis. I am thankful for all of the members of the Ferry group including Pavlos Pachidis, Ian Slauch, John Caputo, Bryan Cote, Christian Pinnell, John Keil, Eleanor Mayes, Rohan Chakraborty, and Maya Ramamurthy for their insightful questions during presentations and allowing me to bounce ideas off of them in the office.

I have also used many of the research facilities on campus. I would like to thank the Characterization Facilities for SEM imaging, the Minnesota Nano Center for electron beam lithography and thermal evaporation, and the Minnesota Supercomputing Institute for computational resources. Moreover, I would like to acknowledge the amazing staff in the CEMS department especially Julie Prince and Teresa Bredahl for their guidance navigating the required administrative paperwork during my time in the program.

I am grateful for the strong network of friends I have made in the my time in the CEMS program. Being able to gather some friends together to play board games was essential to recharge after an exhausting week. In addition I would like to thank my sister and my parents for their unconditional love and support over the past six years.

Abstract

This thesis explores three projects involving the interaction of incident light with nanocrystals: absorption enhancement in patterned quantum dot solids (pQDS), time dynamics of plasmonic nanorod assemblies, and the usage of luminescent solar concentrators (LSCs) to enhance upconversion. First, the effect of nanostructure shape on the absorption in pQDS is studied, and then these structures are integrated with plasmonic nanorings and bullseyes to enhance both absorption and photoluminescence (PL). In the next chapter, the time-dependent optical properties of a gold nanorod assembly is modeled following ultrafast laser illumination, accounting for both changes in the electron density and the nanostructure geometry. Finally, Monte Carlo modeling is used to study the effect of LSCs and mirrors on the absorption and upconverted PL from a hydrogel containing the upconverting donor/acceptor pair PtOEP/DPAS.

Contents

List of Figures

List of Publications

Portions of this thesis have been drawn from the following:

1. Dement, D. B.; Quan, M. K.; Ferry, V. E. Nanoscale Patterning of Colloidal Nanocrystal Films for Nanophotonic Applications Using Direct Write Electron Beam Lithography. *ACS Appl. Mater. Interfaces* **2019,** *11* (16) 14970-14979.

2. Gnabasik, R. A.; Quan, M. K.; Valley, D. T.; Ferry, V. E.; Flannigan, D. J. Direct Imaging of Incoherent-to-Coherent Structural Dynamics in Plasmonic Nanorods with Ultrafast Electron Microscopy. *In preparation* .

Chapter 1

Introduction

1.1 Plasmonics

The field of plasmonics examines the interaction between metallic nanostructures and light at the nanoscale and has found widespread application in areas ranging from sensing to optoelectronics. [1–5] Surface plasmons are the collective oscillation of conduction band electrons at a metal-dielectric interface. [1, 2, 5, 6] These oscillations arise from the coupling of the conduction band electrons to incident light and the restoring force from the coulombic attraction between the conduction band electrons and nuclei of the nanostructure. There are two types of surface plasmons: surface plasmon polaritons (SPPs) and localized surface plasmon resonances (LSPRs). SPPs form when incident light couples to the metal-dielectric surface via nanostructures or gratings that overcome the momentum mismatch. [3, 7] LSPRs can be directly excited due to the confinement of the conduction band electrons to the small nanoparticle volume, resulting in a resonance response across the entire nanoparticle, and they are of interest in this work. [2, 6] These LSPR oscillations form strongly enhanced electromagnetic fields around the nanostructure that can be used to enhance absorption and photoluminescence (PL) of nearby emitters. An example of a LSPR is shown in Figure 1.1

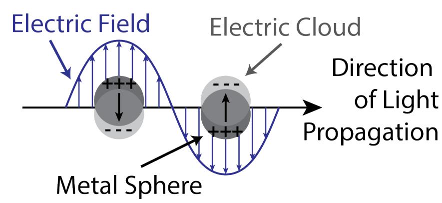

Figure 1.1: Schematic of a localized surface plasmon in a metal nanosphere. Adapted from [8]

This enhanced electromagnetic field is due to the polarizability of the nanostructure. Consider the simplest case in the quasi-static approximation: a nanosphere whose diameter is smaller than the wavelength of incident light. In this limit, the entire nanosphere experiences a uniform electromagnetic field. The polarizability of a spherical particle (α) is a function of the radius (r) and complex dielectric permittivity of the particle (ε) as well as the complex dielectric permittivity of the surrounding environment (ε_1). [1, 2, 5]

$$\alpha = 4\pi r^3 \frac{\varepsilon - \varepsilon_1}{\varepsilon + 2\varepsilon_1} \tag{1.1}$$

The polarizability affects the scattering cross section (C_{scat}), the absorption cross section (C_{abs}), and the extinction cross section (C_{ext}) in this limit, where k is the wavenumber of the incident light. [1, 5, 6]

$$\begin{aligned} C_{scat} &= \frac{k^4}{6\pi} |\alpha|^2 = \frac{8\pi}{3} k^4 r^6 \left| \frac{\varepsilon - \varepsilon_1}{\varepsilon + 2\varepsilon_1} \right|^2 \\ C_{abs} &= kIm\left[\alpha\right] = 4\pi k r^3 Im\left[\frac{\varepsilon - \varepsilon_1}{\varepsilon + 2\varepsilon_1}\right] \\ C_{ext} &= C_{scat} + C_{abs} \end{aligned} \tag{1.2}$$

From these equations, it is apparent that the size, shape, composition, and environment of the nanoparticle all affect its polarizability and thus its optical cross sections. [1, 2, 6, 7, 9] Furthermore, the maximum optical cross section of the plasmonic nanostructures occurs at its resonance wavelength when $\varepsilon + 2\varepsilon_1$ is minimized. By matching the resonance wavelength to the absorption or PL wavelength, the maximum enhancement can be achieved. [1, 2, 5, 6] However, these equations are general and apply to all materials, not just plasmonic materials.

There are a variety of materials used to create plasmonic nanostructures. Noble metals, including gold and silver, are widely used as plasmonic materials due to their low losses, strong resonances, high reflectance across much of the visible range, and resistance to corrosion and oxidation. [6, 10] Aluminum is another plasmonic material used due to its higher reflectivity across the visible range and its natural abundance compared to gold and silver. [11] Some plasmonic ceramic materials, including titanium nitride and zirconium nitride, have been studied for plasmonic applications due to their chemical stability, mechanical strength, and durability compared to the noble metals. [12]

1.2 Quantum Dots

Quantum dots (QDs) have unique optical properties compared to their bulk counterparts due to their small size. QDs have radii less than the exciton Bohr radius of the material, which results in quantum confinement. This changes the band structure of the material from continuous bands in bulk material to discrete band states in QDs. [13–16] A schematic of the band structure for varying QD sizes compared to the bulk material is shown in Figure 1.2(a). As the size decreases, the separation between the lowest discrete state of the conduction band and the highest discrete state of the valence band increases, leading to a larger bandgap and bluer PL. An assortment of QD sizes in solution are shown in Figure 1.2(b).

In addition to the narrow, tunable PL, many QDs have high quantum yields. When a QD absorbs light, it excites a bound electron-hole pair, or exciton. [17] The quantum yield (QY) is the number of photons emitted relative to the number of photons absorbed by the

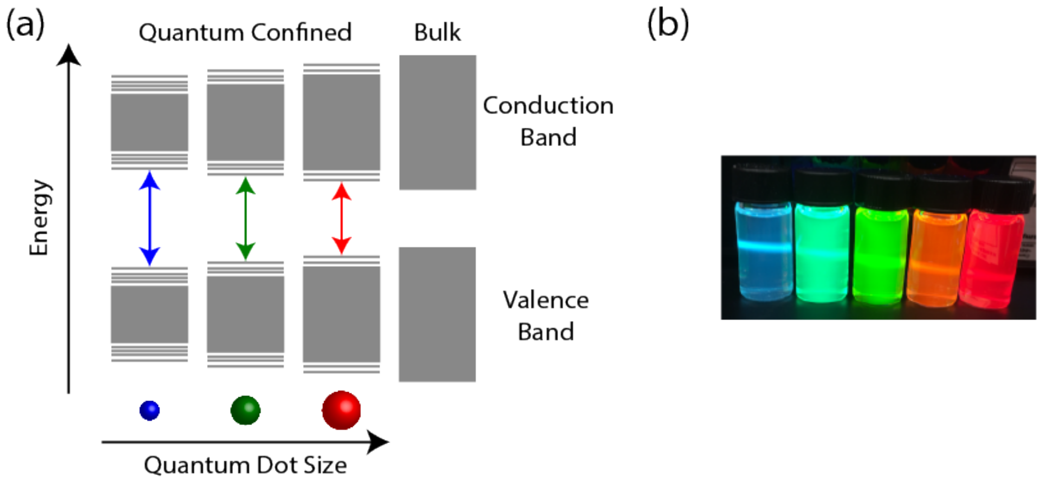

Figure 1.2: Illustration of the size dependent PL wavelength due to quantum confinement. (a) Schematic illustrating the band structure for varying quantum dot sizes compared to bulk. (b) Color image of a range of quantum dot sides excited with an ultraviolet lamp.

QD. It can be defined as:

$$QY = \frac{k_r}{k_r + k_{nr}} \tag{1.3}$$

where k_r is the radiative recombination rate and k_{nr} is the non-radiative recombination rate of the exciton. [15, 17, 18] For near unity quantum yield, k_r should be much larger than k_{nr}, meaning most of the photons absorbed are reemitted. [17, 19] Many have reported quantum yields of at least 70% with some reports of near unity quantum yield. [20–22] The quantum yield of QDs can be further improved through the addition of a passivating shell layer. [23–26] However, there are many non-radiative decay pathways for recombination to occur, limiting the QY. These including impurities and surface states in the QDs that create additional energy levels in the band gap. These levels act as trap states, allowing the excited exciton to step down in multiple steps instead of relaxing in a single PL step. [17, 18, 27, 28] In this work, both CdS_xSe_{1-x}/ZnS core/shell QDs (QDs) purchased from Cytodiagnostics and CdSe/CdS core/shell QDs (QDs) synthesized by Dr. Dana Dement are used.

Another important optical property related to the recombination rates is the fluorescence lifetime, τ. [15, 18, 27, 28] This lifetime measures the average time an exciton is in the excited state. It can be defined as:

$$\tau = \frac{1}{k_r + k_{nr}} \tag{1.4}$$

where k_r is the radiative recombination rate and k_{nr} is the non-radiative recombination rate of the exciton.

Luminescent solar concentrators (LSC) are examined in a later chapter of this thesis. LSCs convert diffuse solar irradiation into a spectrally narrow and directionally emitted PL. [29–34] LSCs can be integrated into building architectures as either semi-transparent or opaque concentrators. [35, 36] LSCs typically consist of a transparent polymer matrix with an embedded luminophore. With high quantum yield and highly tunable optical properties, QDs are commonly chosen as the luminophore. [29, 30, 37–41]. Sunlight is absorbed by the luminophore, emitted, and propagated toward the edge via total internal reflection until it reaches an edge-mounted solar cell. [42] LSCs, therefore, reduce the need for large solar cells by acting as diffuse light concentrators. [43]

1.3 Thesis Outline

Chapter 2 studies absorption in patterned QD solids. The first section explores methods to create patterned QD solids on glass slides and characterizes the optical properties of these solids. Then the effect of pattern shape on the absorption of the QD solid is examined. The patterned QD solids are then integrated with plasmonic rings and bullseyes to enhance absorption and PL.

Chapter 3 explores the optical response of gold nanorod assemblies upon absorption of an ultrafast laser pulse. The first section investigates changes in the size and electron density and the ensuing effect on the extinction cross section for Au nanospheres and Au nanorods. The second section uses finite element modeling to simulate the structural response of Au nanorods on a silicon nitride substrate while accounting for substrate interactions and neighboring nanorod interactions.

Chapter 4 compares various light management devices to increase the absorption and upconverted PL from an air-tolerant upconverting hydrogel. Luminescent solar concentrators are used to spectrally concentrate the incident light, and specular and diffuse mirrors are used to increase the absorption path length. Upconverted PL enhancement out of the hydrogel is further complicated due to the spectral overlap between the upconverted PL and absorption within the luminescent solar concentrator, resulting in a reduction in upconverted PL due to reabsorption losses.

Chapter 2

Absorption Enhancement of Patterned Quantum Dot Solids using Nanoring Assemblies

2.1 Introduction

When QDs are placed in close proximity to one another, they interact with each other, resulting in modified optical properties compared to isolated QDs. [44–48] The QDs can interact with each other via dipole-dipole coupling, where an excited QD induces a dipole moment in a neighboring QD, altering the transition energy of the QD, and resulting in a narrowing of the band gap. [44, 47–49] Alternatively, overlapping electronic wave functions between neighboring QDs results in a transition from discrete energy states to energy bands. [46, 48]

Given that plasmonic nanostructures influence the radiative and non-radiative decay rates of emitters, there has been significant research on the interactions between plasmonic nanostructures and QDs. [1–5] Studies have examined the enhanced PL from both single QD emitters [6, 50–53] as well as continuous QD films, [54–57] but each has its own limitations. With a single emitter, high spatial control allows the placement of the emitter at the peak of the electromagnetic field enhancement, but having only one emitter limits the intensity of PL available for detection. Any misalignment between the plasmonic hot spot and the single emitter location leads to a reduction in the electromagnetic field enhancement of the single emitter. Moreover, emitters in a high intensity electromagnetic field environment over an extended period of time can change their PL properties. Such changes include photobleaching (dyes) and blueshifting of the absorption and PL (QDs), as well as modified radiative decay behavior. [58–61] On the other hand, a continuous film has many more emitters, but the average PL response is weaker because the majority of the emitters experience little electromagnetic field enhancement. By using patterned structures of QD solids, the minimal amount of QDs can be used to maximize the average electromagnetic field enhancement experienced throughout the QD solid. [62]

It is desirable to have strong electromagnetic field enhancement throughout the QD solid. One plasmonic nanostructure that can provide large area electromagnetic field enhancement is the nanoring. Nanorings have been made using a variety of techniques, including colloidal lithography, chemical synthesis, nanoimprinting, and electron beam lithography, and with a wide range of diameters from 100 nm to 10 μm. [10, 58, 63–65] The composition, diameter, and thickness of the nanoring affect the plasmonic resonance and the resulting electromagnetic field profile. It is important to note that imperfections in the fabrication of nanorings can significantly shift the resonances and the electromagnetic field intensities. [66]

With nanoring assemblies, the local electromagnetic field profile is more complex. For example, with a combination of a nanodisk and nanoring, the additional coupling between the dipolar mode of the nanodisk to the higher order modes of the nanoring opens up the previously dark modes to be dipole active. [58, 63, 67–69] This Fano resonance provides another way to interact with emitters in the visible regime for PL enhancement. Varying the center positions of the nanodisk and nanoring results in an asymmetric electromagnetic field profile within the assembly. [58, 69] Concentric nanoring assemblies enable coupling between adjacent nanorings leads to stronger electromagnetic field enhancement near the assembly. [63, 70–73] With concentric nanorings, there is increased tunability compared to a single nanoring using the variation in the gap size between the concentric nanorings. The coupling between the nanorings focuses light towards the center, where the emitter is placed for strong directional PL enhancement. [71, 73]

In this work, the goal is to increase the absorption enhancement within patterned QD solids using the electromagnetic field enhancement from nanoring assemblies. With a robust method to precisely place patterned QD solids, the absorption properties of the QD solid are simulated to understand the shape dependence of absorption compared to a continuous film. The electromagnetic field enhancement from nanoring assemblies is also examined to better understand how the coupling within the nanoring and between adjacent nanorings affects the resulting large area electromagnetic field enhancement. Finally, simulations combining the patterned QD solids and nanoring assemblies are conducted to explore the total absorption enhancement within the patterned QD solids in these large area electromagnetic field enhanced regions.

2.2 Methods

2.2.1 Fluorescence Lifetime Imaging Microscopy

To characterize the PL from the QDs, a fluorescence lifetime imaging microscopy setup is built. Shown in Figure 2.1, the setup couples a PicoQuant 405 nm pulsed laser diode into

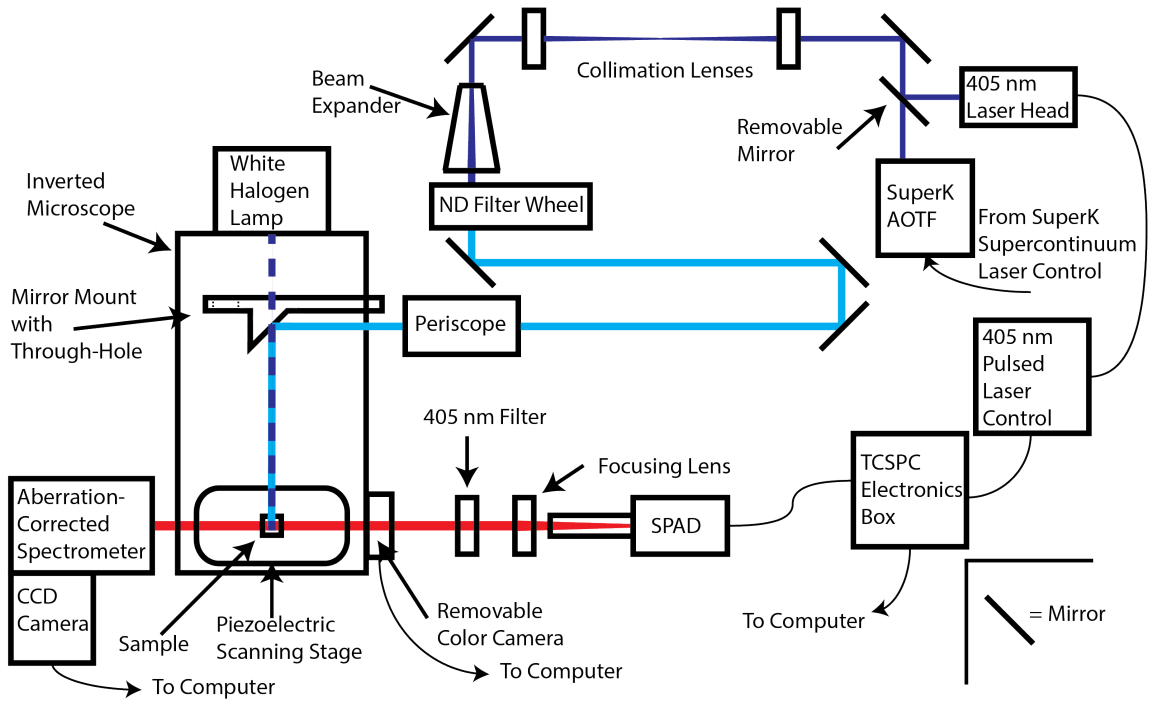

Figure 2.1: Schematic of the home-built laser setup for PL and fluorescence lifetime measurements.

the side port of the Zeiss AxioObserver D1m inverted microscope. For other excitation wavelengths, the EXW-6 SuperK Extreme supercontinuum laser with the acousto-optic tunable filter can be used. Collimating lenses are used to clean up the laser beam before a variable beam expander is used to adjust the laser beam spot size. A ND filter wheel is used to modify the intensity of the laser light used to excite the sample. Using a custom-designed, home-built mirror mount, the laser light is reflected through the microscope and reflected towards the sample using a 405 nm longpass beam splitter. A two-stage setup from Mad City Labs is used to allow for manual positioning with micrometers along with a piezo-controlled nanopositioning stage for high spatial positioning of the laser excitation on the sample. The resulting PL is collected by the objectives and reflected off the imaging beam path switcher. For PL measurements, the PL is sent towards the aberration-corrected and stigmatism-free Isoplane 160 spectrometer and PIXIS:400B digital CCD Camera from Princeton Instruments, which collects PL data using Lightfield software from Princeton Instruments. For color images, a removable AxioCam records images using the Zen imaging software from Zeiss. For fluorescence lifetime measurements, the AxioCam is removed and the PL is focused onto a single photon avalanche diode (SPAD) from MicroPhoton Devices. The SPAD, along with a PicoHarp 300 electronics box and PicoHarp software, is used to collect lifetime data. To allow for a more user-friendly interface, Labview software is used to control the nanopositioning stage, CCD camera, and SPAD for spatially resolved PL and fluorescence lifetime measurements.

To analyze the PL measurements, the PL spectrum is fitted with a Gaussian function to determine the peak wavelength and full width at half max. To analyze the fluorescence lifetime histogram, a stretched exponential model is fit to the fluorescence lifetime:

$$Fit = Aexp\left(-\frac{t}{\tau}\right)^{\beta} + Bkgd \tag{2.1}$$

where A is the amplitude, $Bkgd$ is the background, τ is the fluorescence lifetime, β is the stretching factor ranging from zero to one, representing the variation in lifetime among the excited QDs due to QD size dispersity and environment. [19, 74]

2.2.2 Finite Difference Time Domain Method

Finite Difference Time Domain (FDTD) modeling is used to characterize the interactions between the light and the nanostructures when the size of the nanostructures is on the order of the wavelength of the light. FDTD modeling solves Maxwell's equations [5]:

$$\begin{aligned}
\nabla \cdot \vec{D} &= \rho_{ext} \\
\nabla \cdot \vec{B} &= 0 \\
\nabla \times \vec{E} &= -\frac{\partial \vec{B}}{\partial t} \\
\nabla \times \vec{H} &= \vec{J}_{ext} + \frac{\partial \vec{D}}{\partial t}
\end{aligned} \tag{2.2}$$

where $\vec{D}$ is the dielectric displacement, ρ_{ext} is the external charge density, $\vec{B}$ is the magnetic flux density, $\vec{E}$ is the electric field, $\vec{H}$ is the magnetic field, and $\vec{J}_{ext}$ is the external current density.

In this thesis, the software package Lumerical FDTD Solutions is used. [75] This uses a CAD software to define the nanostructures of interest using the inputs of geometry and complex refractive index of each nanostructure. The complex refractive index is taken either from literature [76] for the plasmonic metals in this work or measured using spectroscopic ellipsometry. A light source and monitors are placed in the simulation space to record how light interacts with the nanostructures. Finally, the mesh size and simulation boundaries are defined before running the simulation.

The FDTD method is used to determine a number of optical properties within the nanostructured system. It can be used to determine the scattering cross section, extinction cross section, absorption, and electric field within nanostructure assemblies. Different light sources and monitors are required to collect the necessary simulated data for post processing in MATLAB.

To determine the scattering and extinction cross sections, a total-field scattered-field (TFSF) light source and transmission monitors are used. Transmission monitors are placed outside the TFSF light source to capture the scattered light off the nanostructure. Transmission monitors are placed inside the TFSF light source but outside of the nanostructure to capture the absorbed light within the nanostructure. By dividing the sum of the power transmitted through the transmission monitors by the intensity of the light source, the cross sections can be determined. The extinction cross section is the sum of the scattering and absorption cross sections.

To determine the absorption calculations, unpolarized plane wave light is used by averaging the simulation results at each polarization. The absorption per unit volume, A_{Vol}, at a position, $\vec{r}$, for an incident photon with angular frequency, ω, can be determined by taking the real portion of the divergence of the Poynting vector, $\vec{P}(\vec{r},\omega)$, which represents the energy flux per unit area. [75]

$$A_{Vol}(\vec{r},\omega) = -\frac{1}{2}\Re\left\{\nabla \cdot \vec{P}(\vec{r},\omega)\right\} \tag{2.3}$$

This can be simplified in terms of the electric field, $\vec{E}(\vec{r},\omega)$,

$$A_{Vol}(\vec{r},\omega) = -\frac{1}{2}\omega|\vec{E}(\vec{r},\omega)|^2\varepsilon''(\vec{r},\omega) \tag{2.4}$$

where $\varepsilon''(\vec{r},\omega)$ is the imaginary component of the dielectric function. Thus, integrating over the volume of the absorbing material results in the total absorption of incident light and normalizing relative to the source power, P_S [77] gives

$$A(\vec{r},\omega) = \int\limits_V -\frac{\omega|\vec{E}(\vec{r},\omega)|^2\varepsilon''(\vec{r},\omega)}{2P_S}dV \tag{2.5}$$

However one limitation of using the FDTD method is the rectangular mesh grid. This is not a problem with rectangular shaped nanostructures as only minor changes to the lengths will occur. For rounded objects like nanodisks, nanospheres, and nanorods, the curves are approximated with a staircasing edge to more closely replicate the shape. However, this can lead to sharper corners or antennas which can significantly change how light interacts with these structures. Smaller mesh sizes can be used to reduce this staircasing effect, but this results in a much longer computational time.

2.3 Creating Patterned QD Solids

2.3.1 Amine Functionalization

One method to create patterned QD solids is through amine functionalization. [78, 79] This chemistry is illustrated in Figure 2.2. To functionalize the glass slide, it is soaked overnight in a 2% v/v solution of (3-Aminopropyl)triethoxysilane (APTES) in spectroscopic grade isopropyl alcohol to create a self-assembled monolayer of primary amine groups on the slide. Simultaneously, carboxyl-terminated ligand CdS_xSe_{1-x}/ZnS core/shell QDs (QDs) from Cytodiagnostics (λ_{emit}= 630 ± 5 nm) are reacted with 1-Ethyl-3-(3-dimethylaminopropyl) carbodiimide (EDAC) in the presence of N-hydroxy-succinimide (NHS) in a 150:10:1 ratio of EDAC:NHS:QD to change the carboxyl-terminated ligands into amide-terminated ligands. Finally, the functionalized glass slide is submerged in the amide-terminated QD ligand solution overnight for the amide and amine react to bind the QDs to the glass surface. The slide is washed with deionized water after being removed from the QD solution to remove any unbound QDs. However, the environment of the QDs has changed significantly from the commercially purchased carboxyl-terminated ligands, to amine-terminated ligands, and finally to being bound on the substrates.

It is important to observe the change in the fluorescence properties of the QDs upon ligand exchange and substrate adhesion because the local environment affects the optical properties of QDs. Figure 2.3(a) illustrates the PL spectra of the QDs in different environments. The commercial carboxyl-terminated ligand QDs have an PL wavelength maximum around 626 nm with a full width at half max (FWHM) of 34 nm. The amide-

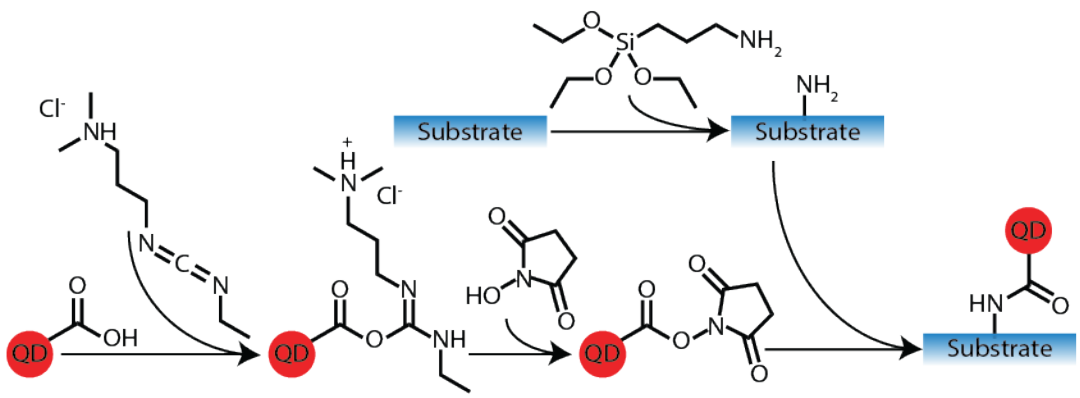

Figure 2.2: Schematic illustrating the dialdehyde click chemistry used to bind carboxyl-terminated QDs to a glass substrate. Adapted from [58].

terminated ligand QDs have little change in PL compared to the carboxyl-terminated ligand QDs ($\lambda_{emit}\sim$ 626 nm, FWHM = 33 nm). Upon binding to the substrate, the QDs show a redshift to 633 nm and a slight broadening to a FWHM of 36 nm relative to the colloidal counterparts. This redshift is expected with the closer proximity of the QDs when bound to the substrate compared to the QDs in solution. Figure 2.3(b) illustrates the fluorescence lifetime histograms of the QDs in different environments. The fluorescence lifetime of the QDs in solution is around 7.6 ns with a beta value of 0.71 for the carboxyl-terminated ligand QDs and 8.8 ns with a beta value of 0.74 for the amide-terminated ligand QDs. Upon adhesion to the substrate, the fluorescence lifetime is 6.6 ns with a beta of 0.75. The relatively constant beta value indicates that the polydispersity of the QDs did not change significantly through the ligand exchange and substrate binding processes. The slight increase in lifetime after ligand exchange is a promising sign of this ligand exchange process. Since the ligand is not removed from the QD, there is no introduction of additional surface defects on the QD from ligands being removed and replaced on the QD. On the contrary, the larger decrease in lifetime upon substrate binding can be attributed to the

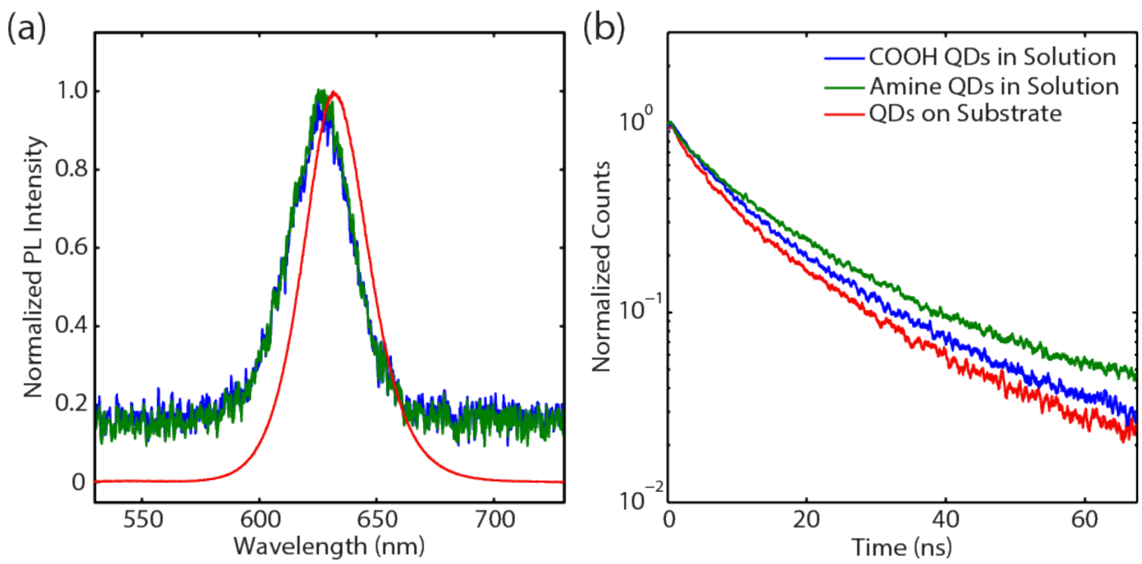

Figure 2.3: (a) PL spectra and (b) fluorescence lifetime histograms comparing carboxyl-terminated QDs in solution, amide-terminated QDs in solution, and QDs bound to the substrate.

closer proximity of the QDs in the solid state. Instead of being isolated to the excited QD, the exciton can transfer to adjacent QDs with more defects where they can be lost nonradiatively. The increase in nonradiatively decay results in a decrease in the measured lifetime.

This amine functionalization method results in the nonspecific binding of QDs to the glass substrate. However, to create targeted QD binding on glass, a substrate masking technique is required. The masking technique needs to use an inert material so that it can be integrated into the amine functionalization method described previously without causing additional chemical reactions with the different QDs, ligands, and solvents.

Electron beam (e-beam) lithography has been used to created the targeted QD patterned shapes and sizes. [58] This is illustrated in Figure 2.4. Briefly, the glass substrate is prepared using a three step cleaning process to remove dust and other contaminants before QD adhesion. First, the substrate is sonicated in acetone, isopropyl alcohol (IPA), and

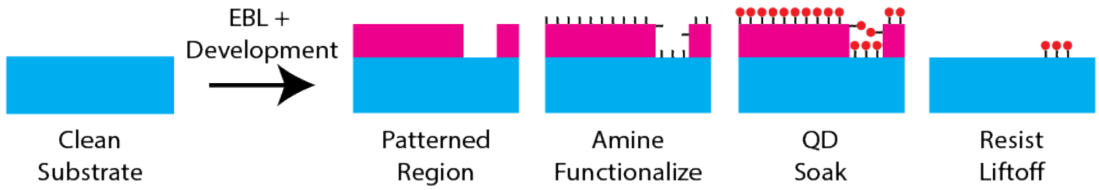

Figure 2.4: Schematic illustrating the use of electron beam lithography to create targeted QD patterns in conjunction with the amine functionalization method.

spectroscopic grade methanol in succession to remove larger particulates. Then, plasma cleaning is used to remove any residual solvent from the sonication. Finally, a 30 minute piranha etch, consisting of a 3:1 v/v solution of 98% sulfuric acid and 30% hydrogen peroxide, is used to fully remove any residual organic material on the substrate. After cleaning, a thin resist layer of PMMA is spincoated onto the substrate followed by the deposition of a sacrificial gold layer for e-beam alignment. Following the e-beam exposure to pattern the desired shapes and sizes, the substrate is developed in a 3:1 IPA:H_2O solution to remove the e-beam exposed PMMA from the unexposed PMMA. The substrate is then dried before being submerged in the APTES solution. This functionalizes both the unexposed PMMA resist and the patterned glass substrate with primary amine groups. The functionalized sample is placed in the amide-terminated QD ligand solution to allow for binding of the QDs to the PMMA and substrate. Finally, the unexposed, functionalized PMMA resist is removed through a two hour soak in spectroscopic grade acetone, leaving only the desired regions of patterned QDs. With this masking process, the desired patterned QD solids are created.

Using this combination of e-beam lithography and amine functionalization techniques, patterned QD solids are created. An example of various triangle patterned QD solids is illustrated in Figure 2.5. The color image shows the PL from these patterned QD solids upon excitation with a 405 nm pulsed laser. The other images show the PL and fluorescence lifetime maps taken with the FLIM setup (described in Section 2.2.1 on page 9) with a step

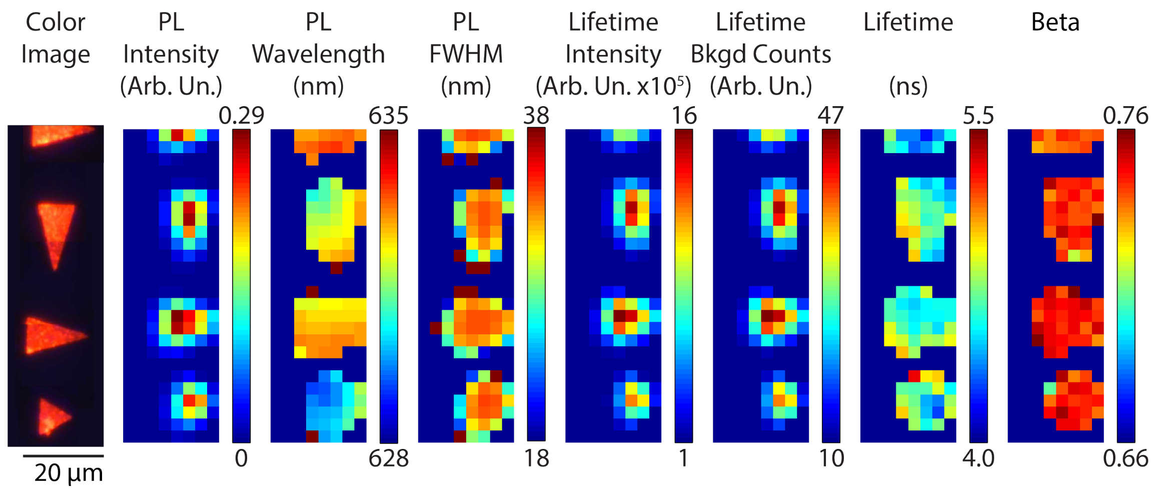

Figure 2.5: Example of patterned QD solids on a glass substrate. Fluorescence image of the patterned QD solids as well as PL and fluorescence lifetime maps measured using the home-built fluorescence lifetime imaging microscopy setup.

size of 3 μm between each measurement. All of the maps show clear separation between adjacent patterned QD solid shapes with regions of low intensity counts separating regions of high intensity counts corresponding to where the QDs are bound to the substrate. Across the majority of these patterned triangles, the PL and fluorescence lifetimes properties are pretty constant. There are some more deviations along the edges of the patterned QDs where the measured intensities are lower than the middle of the patterned QDs. Since the same exposure time is used to record the measurements at each position, fewer photons are collected along the edges of the patterned QD solids, so the fitted parameters shown in Figure 2.5 are more suspect. Nonetheless, this illustrates the ability to create patterned QD solids and characterize them with the FLIM setup.

However, this technique has complications. One limitation of this patterning process arises from the high reactivity of APTES with water. [80] Under prolonged exposure to water in the atmosphere, the APTES in solution aggregates. This aggregation limits the ability of the amide-terminated ligand QDs to bind to the substrate. Furthermore, due to the successive submersion of the substrate in the APTES solution followed by the amide-terminated ligand QD solution, some of the loosely bound APTES molecules can enter the QD solution, binding multiple QDs into a larger QD aggregate. These larger QD aggregates are not able to enter the smaller patterned regions within the PMMA to bind to the substrate, reducing the efficacy of QD adhesion to the substrate. To minimize this problem, the amide-terminated ligand solutions are used only once, which makes this a more wasteful method. Furthermore, with the smaller patterned regions outlined by the PMMA, the high aspect ratio of the PMMA height to the width of the patterned region hinders the transport of QDs to the substrate to be bound. A lower limit of a 100 nm diameter nanodisk is found with this patterning technique. It is possible that further reduction in the patterning size can be achieved with a thinner PMMA resist layer. By reducing the aspect ratio of the patterned PMMA region, it is easier for the QDs in solution to reach the glass substrate to be bound during the allotted time while the substrate is immersed in the QD solution.

Another limitation of this patterning process arises from the incomplete liftoff of unexposed PMMA after the acetone soak. Figure 2.6 shows the fluorescence image excited with the 405 nm laser and the dark field image of scattered white light. It is apparent not all of the unexposed PMMA lifts off cleanly with the acetone wash. This is more apparent in the arrays of varying disk sizes where only some of the disks are clearly defined whereas most of the larger triangle and rectangle shapes are clearly imaged. Further work is needed to consistently lift off the unexposed PMMA so only the desired patterned QD solids remain on the substrate.

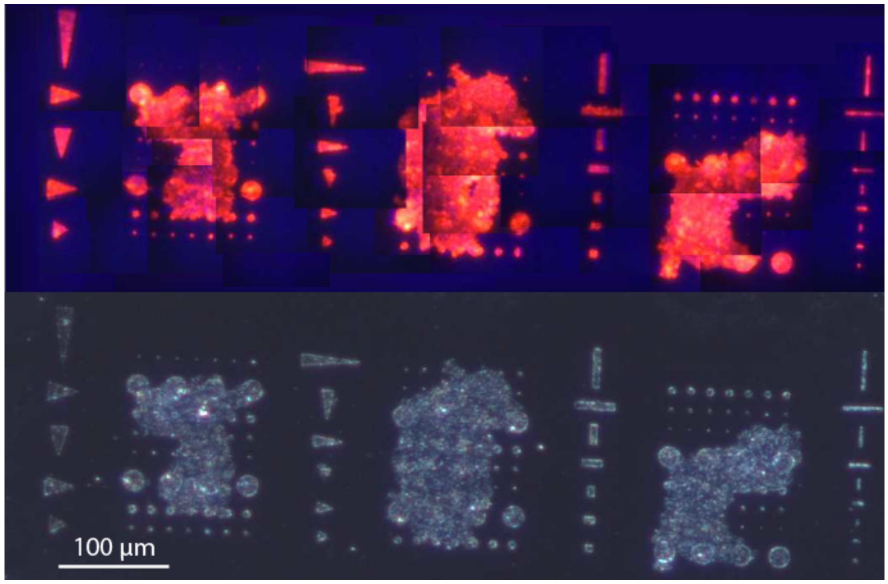

Figure 2.6: Fluorescence and dark field images of patterned QD solid arrays of various sized disks, triangles, and rectangles after acetone liftoff.

2.3.2 Simulated Scattering Cross Section and Absorption in Patterned QD Solids

Recent work by Dr. Dana Dement uses a direct write electron beam lithography as an alternative method to precisely place and define nanoscale patterns of QDs. [81] In this technique, the QDs are used as the resist material, such that exposure to an electron beam cross-links the ligands. Rinsing with the original solvent removes the unexposed regions. This technique creates robust, nanoscale patterns with feature sizes as small as 30 nm. Aligned writes can also be performed to create more complex designs that incorporate metallic nanostructures or multiple layers of QDs.

These nanocrystal solids are comprised of both the individual QDs and the shape defined by the electron beam exposure. Three nanostructure shapes are simulated to examine the changes in the scattering cross section of these QD nanostructures with varying size and incident wavelength. Figure 2.7 shows the scattering cross section normalized by the geometric

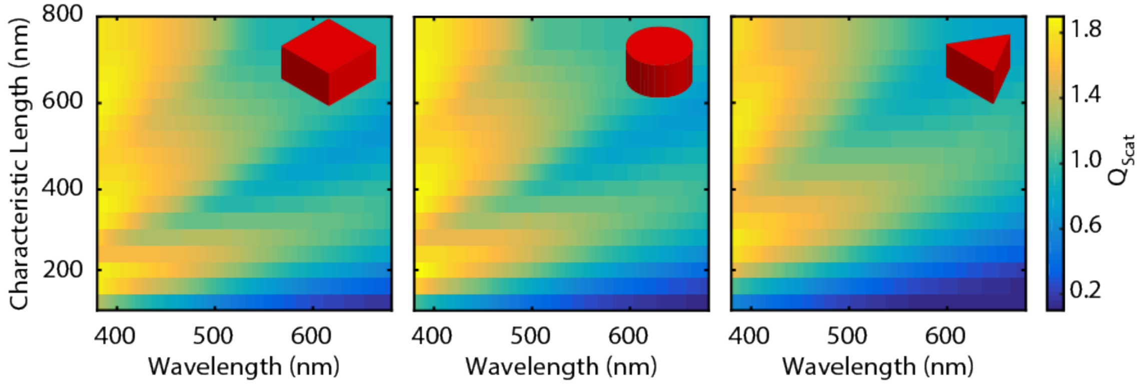

Figure 2.7: Simulated scattering cross section of 130 nm tall patterned QDs of squares, disks, and triangles. The characteristic length is the side length of the square and triangle and the diameter of the disk. Adapted from [81].

cross section of the three different nanostructure shapes at varying characteristic lengths. The complex refractive index used to simulate the QD nanostructures is the experimentally measured complex refractive index determined from spectroscopic ellipsometry. [81] The characteristic length is the side length for the square and triangle nanostructures and the diameter for the disk nanostructures. The simulated scattering cross section modes redshift with increasing characteristic length. Moreover, the scattering cross section is largest where the QDs absorb ($\lambda < 600$ nm), but is still present at longer wavelengths. Focusing on the high scattering cross section band at the lower characteristic length, it is apparent the slope of this band is steepest for the triangle nanostructures and shallowest for the square nanostructures. This indicates that, for a fixed characteristic length, a longer wavelength can resonate within the square compared to the disk, whereas a shorter wavelength resonates within the triangle. This shape and size dependence indicates the resonant modes observed are likely the Mie resonance modes for these QD nanostructures.

To gain further insight into how the shape affects the optical properties of the QD nanostructures, the fraction of incident light absorbed within the nanostructures is com-

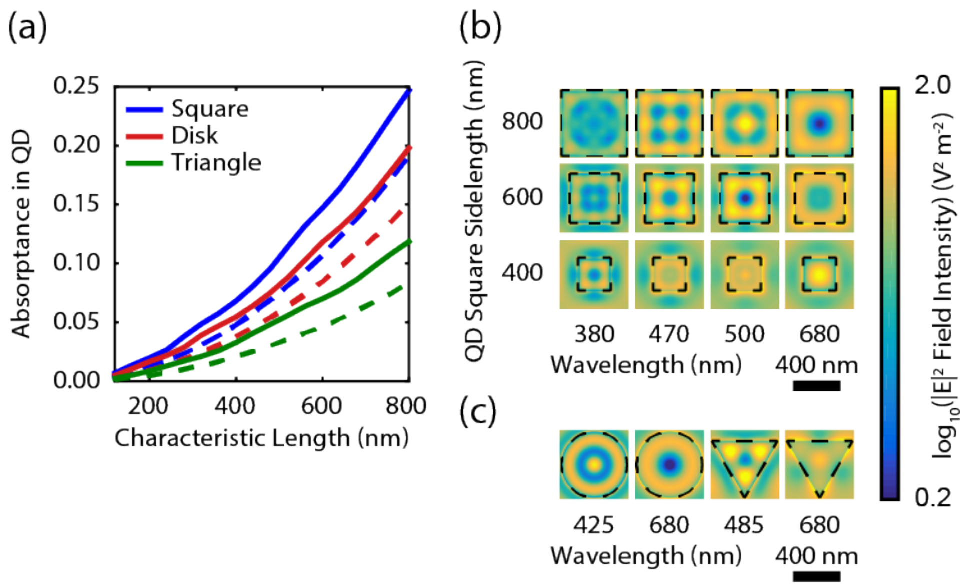

Figure 2.8: Simulated absorption and electric field profiles in 130 nm tall patterned QDs of squares, disks, and triangles at 404 nm. (a) Comparison of the fraction of light absorbed in the patterned QD solid (solid line) versus an equivalent volume region of a QD film (dashed line). Electric field intensity cross sections of (b) select patterned QD square nanostructures and (c) select patterned QD disks and QD triangle nanostructures. The black dashed lines outline the edges of the patterned QD solids. Adapted from [81].

pared to the absorption in an equivalent volume region determined from simulations of a continuous QD film in Figure 2.8(a). For all three shapes, the fraction of light absorbed in the nanostructure exceeds the fraction of light absorbed in an equivalent volume region of a continuous QD film. This increase in absorption in the QD nanostructure due to the effect of the shape of the nanostructure can be explained again by the Mie resonance modes generated within the patterned nanostructures described previously. For the continuous film, the electric field intensity only varies in the direction of light propagation, which, for these simulations, is along the axis of the nanostructures. The average electric field intensity within the QD nanostructure is higher than the average electric field intensity in an equivalent volume region of a continuous QD film. Since the absorption is directly proportional to the electric field intensity (Equation 2.3 on page 13), there is more absorption in the QD nanostructures.

Finally, the Mie resonance modes in the nanostructures are visualized with cross sections of the electric field intensity profiles. Figure 2.8(b) illustrates selected electric field intensity cross sections of square nanostructures. By tuning the size and wavelength of incident light, different modes can be excited within the QD square nanostructure, as illustrated in the electric field intensity cross sections. These different modes are dictated by the size of the nanostructures and the wavelength of incident light. Figure 2.8(c) illustrates a few select modes within the QD disk and triangle nanostructures. Looking at the modes within various shapes illustrates the role the nanostructure has on the optical properties. The higher electric field intensities can be localized to the edges or corners of the nanostructure or in the center of the nanostructures. This localization can be used for further QD nanostructure design for enhanced absorption and PL applications.

2.4 Simulated Electric Field Enhancement within QD Solids using Plasmonic Nanorings

With this robust method to create patterned QD solids and a better understanding of the optical properties of individual QD nanostructures, the next step is to integrate plasmonic nanostructures to further increase the absorption enhancement. Upon addition of plasmonic nanorings around the patterned QD nanostructures, the electromagnetic field profile is further convoluted with the resonances due to the structure and composition of the nanorings. Thus, a thorough investigation into the nanoring structure and composition is required to understand how they can be used to increase absorption within the patterned QD nanostructure.

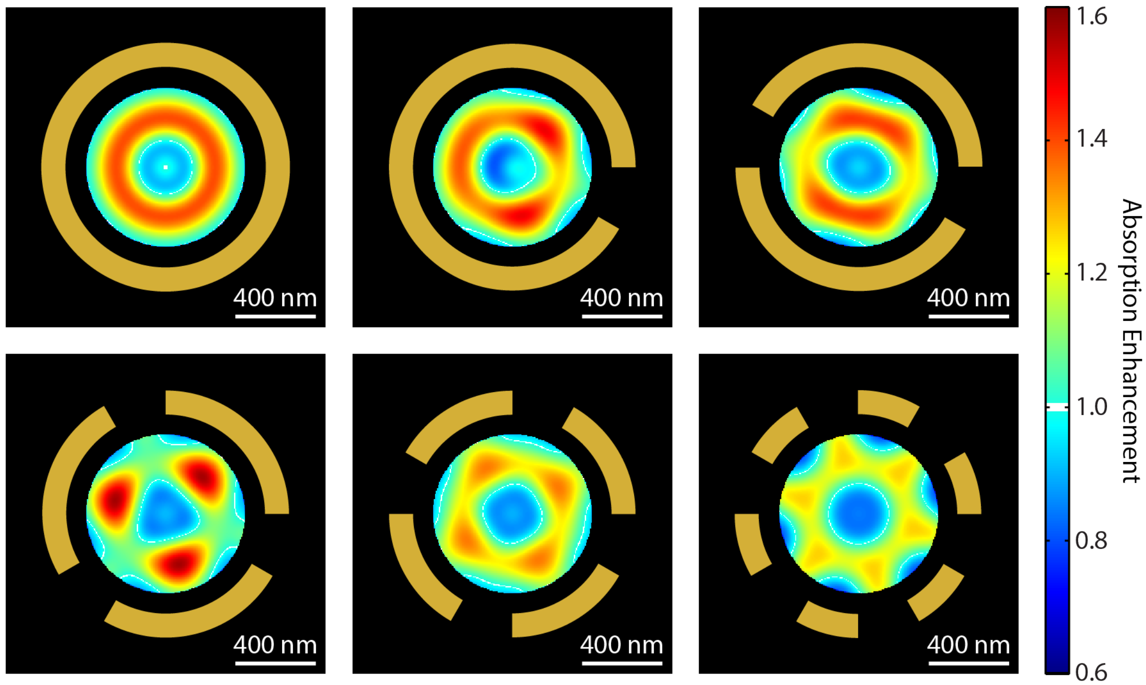

Figure 2.9: Absorption enhancement at 405 nm within a 800 nm diameter patterned QD nanodisk due to the presence of gold nanoring pieces.

Figure 2.9 illustrates the absorption enhancement within a patterned QD nanodisk due to the presence of the Au nanoring. Different nanorings that contain different numbers of breaks are examined. Compared to the absorption of only the patterned QD nanodisk, the continuous Au nanoring leads to an absorption enhancement factor of 1.18. With more breaks in the nanoring, the absorption enhancement decreases to 1.10 with six breaks. Though the full nanoring provides the largest absorption enhancement factor when considering the entire patterned QD nanodisk, breaks in the nanoring can be used to localize higher electric field intensities within the nanoring structure that can be used in conjunction with smaller patterned QD structures for enhanced absorption and PL.

One important consideration is the composition of the nanoring. Figure 2.10 shows the absorption enhancement within the patterned QD nanodisk with varying nanoring

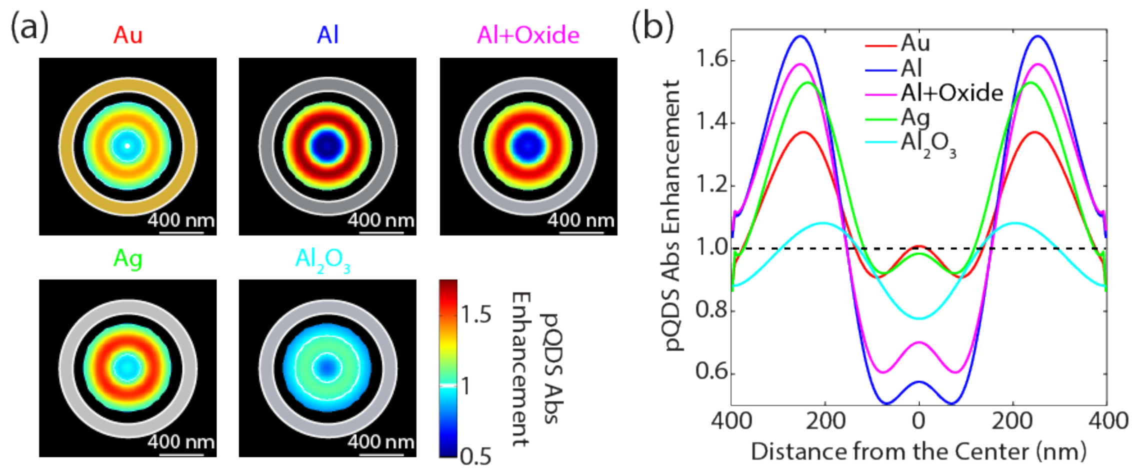

Figure 2.10: Absorption enhancement at 405 nm within a 800 nm diameter patterned QD nanodisk with varying nanoring composition. (a) Cross section of the absorption enhancement through the middle of the nanodisk in different nanoring environments. (b) Diameter cross section of the corresponding nanoring variations in (a).

composition. The same size nanoring and patterned QD nanodisk are examined. The alumina nanoring shows the lowest absorption enhancement factor of 0.97 within the patterned QD nanodisk since alumina is not plasmonic. Moreover, variations in the absorption enhancement across the patterned QD nanodisk are relatively small. The aluminum nanoring provides the largest absorption enhancement factor of 1.32 along with the largest variation in the absorption enhancement across the patterned QD nanodisk. Upon inclusion of the alumina oxide layer on the aluminum nanoring, the absorption enhancement factor decreases slightly to 1.29 due to the passivation of the exposed aluminum nanoring. The silver nanoring provides an absorption enhancement factor of 1.27, slightly lower than the aluminum nanoring case as noted by the lower absorption enhancement in the annulus region approximately 250 nm from the center of the patterned QD nanodisk. However, the middle of the patterned QD nanodisk does not have as significant of a drop in absorption as the aluminum nanoring system. All of these plasmonic metals show larger absorption enhancement than the gold nanoring. Among all of the plasmonic materials examined,

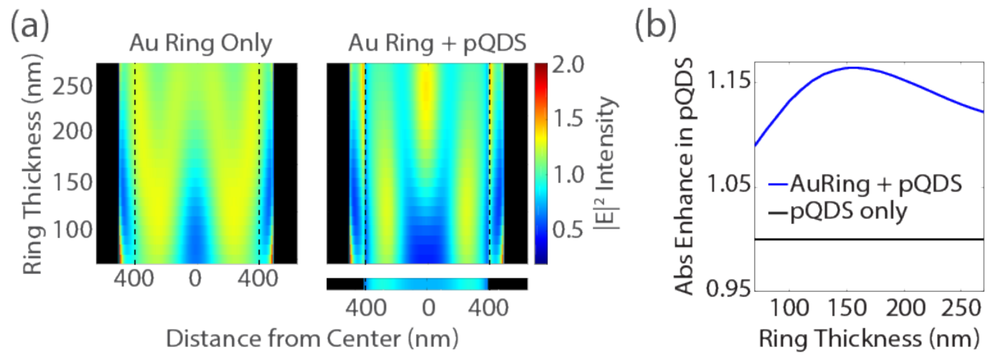

Figure 2.11: Variation in gold nanoring thickness with a fixed 100 nm gap size between the 800 nm diameter patterned QD nanodisk and the gold nanoring thickness. (a) Electric field intensity within the gold nanoring with and without the patterned QD nanodisk. The electric field intensity of only the patterned QD nanodisk is shown below for reference. (b) Absorption enhancement within the patterned QD nanodisk due to the presence of the gold nanoring with various thicknesses.

gold has a more uniform absorption enhancement across the entire patterned QD nanodisk, illustrating the tradeoff between higher total absorption enhancement and a uniform electric field enhancement across the patterned QD nanodisk.

The thickness of the nanoring also plays an important role in the electromagnetic field profile within the nanoring. Varying the coupling distance between the inner diameter and outer diameter of the nanoring results in different electromagnetic field profiles that can enhance absorption within the patterned QD nanodisk. The thickness of the gold nanoring is varied from 70 nm to 270 nm while the gap size between the patterned QD nanodisk and inner diameter of the gold nanoring is fixed at 50 nm. The same 800 nm diameter patterned QD nanodisk is used in these simulations. Figure 2.11(a) shows the electric field intensity within the gold nanoring with varying nanoring thickness. With increasing nanoring thickness, there is a gradual change from the single annulus of higher electric field intensity surrounding a center of low electric field intensity to an annulus of lower electric field intensity surrounded by an annulus and a center of higher electric field intensities. Upon inclusion of the patterned QD nanodisk, a different electric field profile arises due to the combined effects of the nanoring thickness and Mie resonances of the patterned QD nanodisk. The electric field profile within the patterned QD nanodisk with no nanoring structure in the lower right of Figure 2.11(a) shows an annulus of higher electric field intensity surrounding a center of lower electric field intensity. Upon the addition of a thin (70 nm) gold nanoring, the larger difference in the electric field intensity between the annulus and center is observed with the increase in electric field intensity in the annulus and decrease in electric field intensity in the center. Around a nanoring thickness of 130 nm, the emergence of a higher electric field intensity center splits the lower electric field center into a lower electric field annulus sandwiched between the newly higher electric field center and the original higher electric field annulus. Summing the absorption within the patterned QD nanodisk across the absorbing wavelengths and comparing the absorption to a patterned QD nanodisk with no gold nanoring, the absorption enhancement within the patterned QD nanodisk with nanoring thickness is shown in Figure 2.11(b). This results in a maximum absorption enhancement factor of 1.17 at a nanoring thickness of 160 nm. Across the range of nanoring thicknesses examined, a minimum absorption enhancement factor of 1.09 is determined even with the thinnest nanoring thickness of 70 nm. With the variation in nanoring thickness at a constant nanoring inner diameter, there is a gradual change in the electric field profile within the patterned QD nanodisk. With increasing nanoring thickness, the annulus of higher electric field slowly moves towards the inner diameter of the nanoring, leading to the decrease in the absorption enhancement beyond a nanoring thickness of 160 nm.

The inner diameter of the nanoring also plays an important role in determining the electromagnetic field profile within the nanoring. Varying the inner diameter of the nanoring affects the resulting electromagnetic interference profile within the nanoring. With a fixed gold nanoring thickness of 120 nm, the gap space between the outer diameter of the patterned QD nanodisk and the inner diameter of the gold nanoring is varied from 50

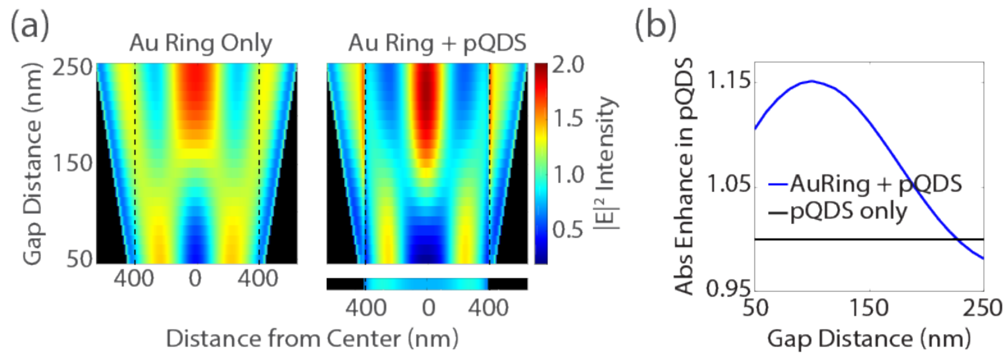

Figure 2.12: Variation in the gap space between the inner diameter of the 120 nm thick gold nanoring and 800 nm diameter patterned QD nanodisk. (a) Electric field intensity within the gold nanoring with and without the patterned QD nanodisk. The electric field intensity of only the patterned QD nanodisk is shown below for reference. (b) Absorption enhancement within the patterned QD nanodisk due to the presence of the varying gap space between the gold nanoring and patterned QD nanodisk.

nm to 250 nm, resulting in the inner nanoring diameter variation between 800 nm to 1300 nm. Figure 2.12(a) shows the electric field intensity within the nanoring with varying gap space. Compared to the variation in nanoring thickness examined previously, varying the gap size at constant nanoring thickness has a larger effect on the electric field intensity within the nanoring. At all sizes, there is an annulus of lower electric field intensity at the inner diameter edge of the nanoring. At a smaller gap distance, there is an annulus of higher electric field surrounding a center of lower electric field. Around a gap distance of 130 nm, there is a more uniform distribution of higher electric field intensity across the center of the nanoring. At larger gap distances, the electric field profile develops into a center of highest electric field intensity surround by concentric annuli of lower then higher electric field intensity followed by the lower electric field intensity at the inner diameter edge of the nanoring. This increase in the electric field oscillations with increasing inner diameter is explained again by the interference of reflected light waves within the nanoring. With increasing inner diameter, a larger number of periods of the interference light pattern persist in the nanoring. Upon addition of the patterned QD nanodisk, the electric field within the patterned QD nanodisk narrows. This can be explained by the perceive reduction in wavelength in the higher refractive index QD nanodisk compared to air. At small gap distances, a similar profile of a higher electric field intensity annulus surrounding the central lower electric field intensity is observed. However at larger gap distances, this inverts where the lower intensity electric field annulus surrounds a higher electric field intensity center. This results in a larger change in the absorption enhancement within the patterned QD nanodisk, as shown in Figure 2.12(b). The absorption enhancement factor peaks at 1.15 for a gap distance of 100 nm. However, at large gap distances, the absorption enhancement factor drops to 0.98 at a 250 nm gap distance. Thus, the variation in the inner diameter of the nanoring has a larger impact on the absorption enhancement within the patterned QD nanodisk than the variation in nanoring thickness.

2.5 Simulated Electric Field Enhancement within QD Solids using Embedded Aluminum Nanoarrays

With a better understanding of the electric field intensity from a single nanoring, the next step is to examine the electric field intensity around nanoring assemblies. Noting the largest electric field intensity enhancements with the aluminum nanoring compared to the other plasmonic metals examined, they are used here. Aluminum nanoring assemblies are embedded in a layer of alumina so the patterned QD solids can be placed on top of the flat alumina surface as illustrated in Figure 2.13. Here the oxidation of the aluminum nanostructures is less of a concern. The three nanorings sizes examined have outer/inner diameters of 280/240 nm, 200/160 nm, and 120/80 nm. The concentric nanoassembly therefore has 20 nm thick nanorings and 20 nm gap spacing between the nanorings. The

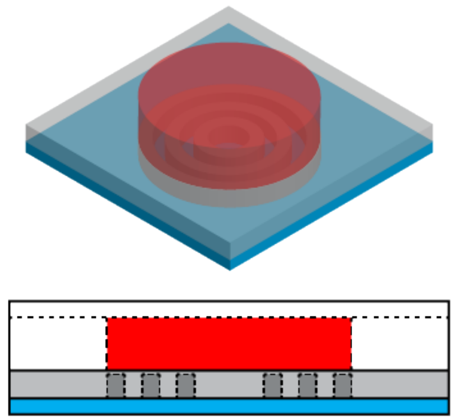

Figure 2.13: Schematic illustrating the aluminum nanoring assembly embedded in an alumina layer with a patterned QD nanodisk above the nanoring assembly.

pitch between the nanostructures is 500 nm. With this large pitch compared to the largest outer diameter, there is no coupling interaction between neighboring nanoring assemblies. In these systems, the objective is to increase the electric field intensity above the nanoring assemblies where the patterned QD solids are located.

To start this investigation, the simplest case of three concentric aluminum nanorings embedded in alumina with a continuous QD film above the alumina is examined to better understand the coupling interactions between concentric nanorings and the resulting electric field intensities. The increase in absorption in the QD film with the concentric nanorings is much larger than the increase in absorption in the QD film with the individual nanorings. Figure 2.14(a) illustrates the absorption within the above QD film in the presence of the embedded concentric nanorings and individual nanorings. Looking at the individual nanorings, there is not a significant increase in absorption across the absorbing wavelengths of the QD film compared to the system with no aluminum nanorings. However, with all three concentric nanorings, there is a significant increase in absorption within the QD film across the majority of the absorbing wavelengths. This is greater than the sum of the

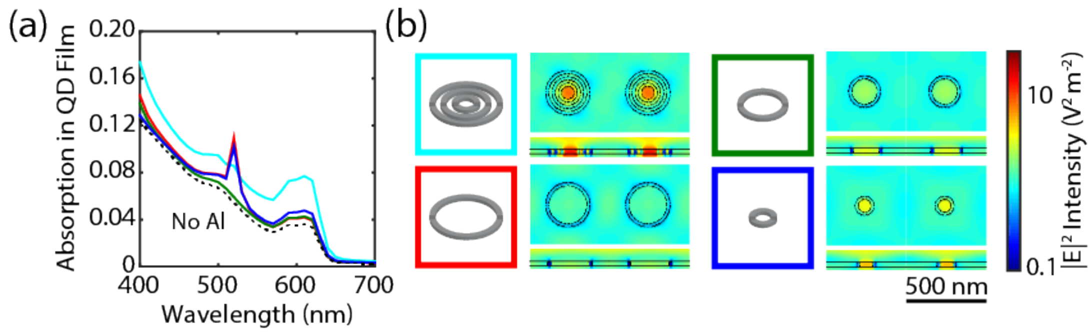

Figure 2.14: Absorption in the QD film and electric field intensity cross sections of an array of embedded concentric aluminum nanoring assemblies. (a) Absorption in the QD film above the assembly for the concentric nanoring assembly and the individual nanorings. A reference QD film absorption spectrum is illustrated in the black dashed line. (b) Electric field intensity cross sections for the concentric nanoring assembly and three individual nanorings. The colored box around each schematic corresponds to the absorption spectra of these four nanoring assemblies in (a).

individual absorption increases from the individual nanorings, illustrating the beneficial effect of the interaction between the nanorings to generate a higher electric field intensity above the nanorings. The electric field cross sections are shown in Figure 2.14(b). The concentric nanoring assembly and the individual nanoring schematics are colored to match the absorption spectra in Figure 2.14(a). Looking at the electric field cross sections along the diameter of the nanorings, it is clear the electric field intensity above the nanorings is focused primarily over the center of the nanoring assemblies. However, much of the higher electric field intensity resides within the inner diameter of the nanorings, in the alumina layer. To further increase the absorption within the above QD film, it is imperative to find other plasmonic nanostructures to shift these higher electric field intensities from the alumina layer into the QD film.

However, looking at the absorption in the above QD film, a narrow absorption peak is seen around 520 nm for only the largest and smallest nanorings. One possible explanation for this narrow absorption peak is the generation of a Fabry Pérot mode between the

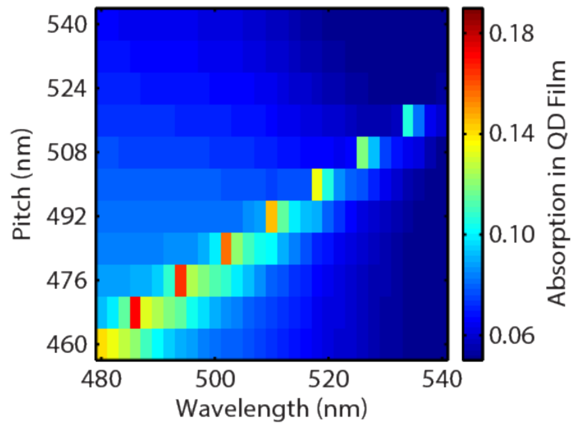

Figure 2.15: Absorption in the QD film above the largest aluminum nanoring array with varying pitch.

outer diameters of the nanorings in their respective arrays. These modes are sensitive to the distance between the outer diameters of the nanoring and the pitch of the array. To further examine the pitch dependence of this narrow absorption peak, arrays of the largest nanoring are simulated at different pitches. Figure 2.15 illustrates the absorption in the QD film above the largest nanoring at varying pitch. With increasing pitch, the sharp peak in absorption redshifts, which confirms the peak observed at 520 nm for the 500 nm pitch for the largest nanoring and smallest nanoring in Figure 2.14(a) is a function of the pitch of the nanoring array. This reaffirms the wavelength and pitch dependence on the Fabry Pérot mode between the arrays of the large and small nanorings.

With the origin of the narrow absorption peak resolved, the problem of the higher electric field intensities residing within the alumina layer remains. One method to move this higher electric field intensity up into the QD film is through the use a central aluminum nanodisk instead of a central aluminum nanoring. A 120 nm diameter nanodisk is used in place of the 120/80 nm outer/inner diameter nanoring. Figure 2.16(a) shows the absorption in the QD film for the concentric nanoring assemblies with the central nanodisk and central nanoring. Across the absorbing range of the QDs, the inclusion of the central nanodisk increases the

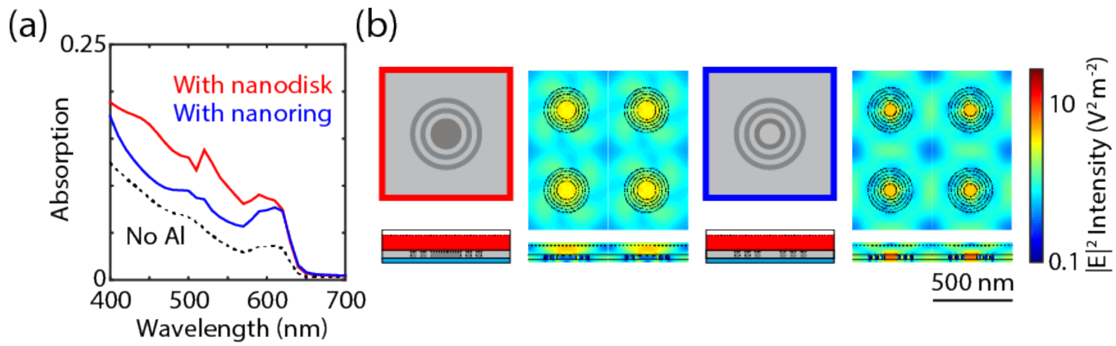

Figure 2.16: Absorption in the QD film and electric field intensity cross sections of an array of embedded concentric nanoring assemblies with a central nanodisk and a central nanoring. (a) Absorption in the QD film above the two assemblies. (b) Electric field intensity cross sections for the concentric nanoring assemblies.

absorption in the above QD film. Figure 2.16(b) shows the electric field intensity profile in the QD film with the corresponding diameter cross section through the nanoassembly. The higher electric field intensities above the central nanodisk compared to the electric field intensity above the central nanoring results in the increased absorption observed. The diameter cross sections more clearly highlight the higher electric field intensity in the QD film above the nanoassembly with the central nanodisk compared to the higher electric field intensity in the alumina layer in the center of the central nanoring. With this promising nanodisk-centered nanoring aluminum assembly, the next step is to integrate the patterned QD nanodisks studied previously to understand how the combined effects of the shape of the QD nanodisks and the underlying plasmonic nanoassembly result in absorption enhancement within the QD nanodisks.

To quantify the absorption enhancement within the patterned QD nanodisks due to the presence of the aluminum nanoassembly with the central nanodisk, the absorption within the patterned QD nanodisks is compared with and without the nanoassembly. Figure 2.17(a) illustrates the electric field intensity profiles around the nanoassembly at select patterned QD nanodisk diameters. The corresponding profiles with the continuous film

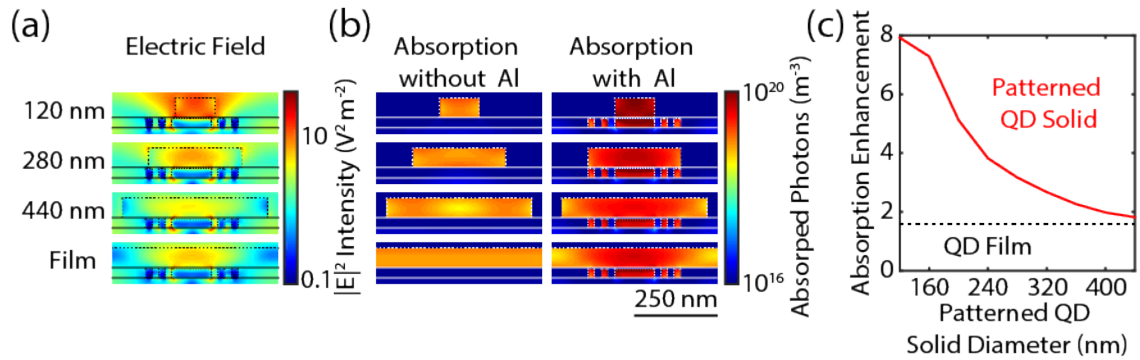

Figure 2.17: Cross sections of electric field intensity and absorption per unit volume of patterned QD nanodisks and a continuous QD film. (a) Electric field intensity profiles of the concentric nanoring assembly with a central nanodisk with varying patterned QD nanodisk diameters and a continuous QD film. Dashed lines outline the edges of the patterned QD nanodisks. (b) Absorption per unit volume profiles of varying patterned QD nanodisk diameters and a continuous QD film with and without the aluminum nanoassembly. (c) Absorption enhancement within the patterned QD nanodisk with varying patterned QD nanodisk diameter. The absorption enhancement within the continuous QD film is illustrated in the dashed line for reference.

is also illustrated for this array with a 500 nm pitch. With the smallest patterned QD nanodisk diameter of 120 nm, high electric field intensities are found in the patterned QD nanodisks. With larger patterned QD nanodisk diameters, the electric field intensity is lower on average throughout the nanodisk. The electric field profiles also approaches that of the continuous film as illustrated with the largest diameter of 440 nm. The absorption profiles with the aluminum nanoassembly shown in 2.17(b) mirror the results seen in the electric field intensity profiles since the electric field intensity and absorption per unit volume are directly proportional to one another.

Interestingly, looking at the absorption within the patterned QD nanodisks with and without the embedded aluminum nanoassembly, there is a clear shift in the regions where there is stronger absorption. Without the embedded aluminum nanoassembly, the shape of the patterned QD nanodisks play a larger role in determining the location of higher absorption within the patterned QD nanodisk. This disappears once the edges disappear in the continuous film system and the absorption profile only varies with height in the QD film. With the embedded aluminum nanoassembly, the strong electric field concentration above the nanoassembly results in increased absorption centered above the nanoassembly. This is most apparent in the 440 nm diameter QD nanodisk where there is an annulus region of a higher number of absorbed photons, but upon inclusion of the aluminum nanoassembly, the strong electric fields from the assembly result in a large central region of higher number of absorbed photons as illustrated in 2.17(b).

To quantify this absorption enhancement, Figure 2.17(c) illustrates the absorption enhancement of the patterned QD nanodisk at varying diameters with the comparison to the continuous QD film for the pitch size of 500 nm. With the smallest patterned QD nanodisk examined, an absorption enhancement factor of 8.0 can be achieved due to the high electric field intensities directly above the central nanodisk, which is where the patterned QD nanodisk resides. With increasing size, larger fractions of the patterned QD nanodisk experience a lower electric field intensity compared to the region just above the aluminum nanodisk, which results in the rapid decrease in absorption enhancement factor with increasing patterned QD nanodisk diameter. Finally with larger diameters, the absorption enhancement factor approaches that of the QD film as the QD coverage approaches that of the continuous QD film. From these results, it is clear the strong electric fields generated by the aluminum nanoassembly dominate the absorption enhancement within the patterned QD nanodisk.

Although the inclusion of the embedded aluminum nanoassembly dominates the absorption enhancement within the patterned QD nanodisk, the shape effects of the patterned QD nanodisk are still present. Using the similar approach to compare the shape effects of the patterned QD nanodisk without the presence of the aluminum nanostructures illustrated in Figure 2.8 on page 22, Figure 2.18 compares the absorption within the patterned QD nanodisk to the absorption in an equal volume region of the continuous QD film. Regions of

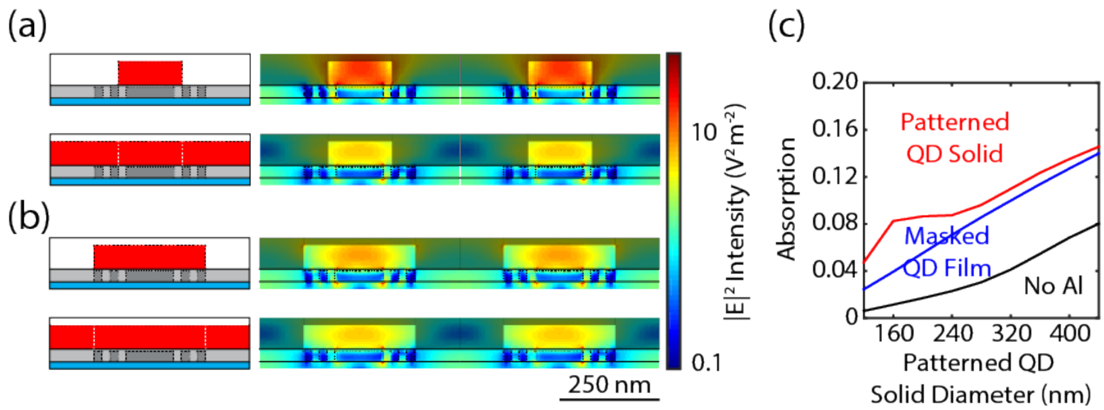

Figure 2.18: Cross sections of electric field intensity and absorption within the patterned QD nanodisks compared to an equivalent volume region of a continuous QD film. Comparison of the electric field intensity cross section for a patterned QD nanodisk and an equivalent volume region of a continuous QD film for a patterned QD nanodisk diameter of (a) 160 nm and (b) 280 nm. Part of the electric field intensity profiles are shaded to better visualize the sizes of the patterned QD nanodisk for easier comparisons to the equivalent volume region of a continuous QD film. (c) Absorption within the QD nanodisk with varying patterned QD nanodisk diameter for the patterned QD nanodisk with the aluminum nanoassembly, the equivalent volume region of a QD film with the aluminum nanoassembly, and the patterned QD nanodisk with no aluminum assembly.

the electric field cross sections are shaded to more clearly compare the increased electric field intensities within the patterned QD nanodisk compared to the equivalent volume section of the continuous QD film. For the smaller 160 nm diameter QD nanodisk (Figure 2.18(a)), there is a stronger electric field intensity in the patterned QD nanodisk compared to the equivalent region in the continuous QD mask. With a larger 280 nm diameter (Figure 2.18(b)), the differences between the electric field intensities are less pronounced compared to those in the smaller diameter system. These higher intensity electric field profiles lead to the increased absorption within the patterned QD nanodisk at all diameters simulated in Figure 2.18(c). It is clear the finite sizes of these patterned QD nanostructures contribute towards the increased absorption within the QD nanostructures both with and without plasmonic nanostructures (Figure 2.8(a)).

Through this investigation of embedded aluminum nanoassemblies and the simulated absorption enhancement of the above film, three key points can be drawn. First, the coupling effects between concentric nanorings results in a stronger electric field intensity above the nanoassembly than the combined electric field intensities of the individual nanorings. Second, the use of a central nanodisk results in higher electric field intensity above the nanoring assembly than the use of a central nanoring for increased absorption enhancement within the patterned QD nanodisk. Lastly, the aluminum nanoassembly provides the majority absorption enhancement within the patterned QD nanodisk, while the Mie resonance modes that arise from the geometry of the patterned QD nanodisk provide a lesser, but not negligible amount of absorption enhancement within the patterned QD nanodisk.

Chapter 3

Modeling the Response of a Gold Nanorod Cluster Following Ultrafast Laser Illumination

3.1 Introduction

Plasmonic nanoparticles excited with ultrafast laser pulses generate unique, time-dependent optical and structural responses. They are commonly studied using pump-probe far-field all-optical techniques to unravel the influence of structure, morphology, and particle-particle contacts on the plasmonic nanoparticles following photoexcitation. [82–88] Changes in the plasmon resonance are detected as oscillations in the optical signal, which correspond to the changing lattice of the nanoparticle. Monodisperse samples are required to minimize ensemble averaging effects on the optical response which obfuscate dynamics because of the sensitivity of the optical response to shape and geometry of the nanostructure. Optical single-nanostructure measurements eliminate the ensemble effect, but instead require nontrivial models to interpret and induced plasmonic and structural dynamics found in assemblies. [89–93] However, all-optical techniques are diffraction limited, which limits the detection spot size for single particle and assembly measurements, and cannot detect dynamics that may be due to sample variation. Assemblies also complicate interpretation of the measurements, as variation in coupling between particles can also cause spectral shifts. As a result, the understanding of the energy relaxation timeline from non-thermal electrons to acoustic modes and the critical dependencies on intra-particle defects, surface morphology, particle-particle interactions, and particle-substrate interactions is poorly understood. [94–96] Recent work has used techniques like Bragg coherent diffraction imaging [97] and ultrafast transmission electron microscopy to provide spatio-temporal resolution, and to directly characterize the structural response following ultrafast laser excitation by observing coherent oscillations in plasmonic nanostructures. [98, 99]

Briefly, the laser is absorbed and generates a nonthermal electron distribution in the first 50 fs. Electron thermalization occurs in the next 500 fs through electron-electron scattering. In 1-5 ps, electron-phonon scattering occurs to transfer energy from the hot electrons to the cold lattice, thermalizing and equalizing the temperatures of the electrons and lattice. Finally, the lattice and the surrounding medium interact through acoustic oscillations from hundreds of ps to ns to dissipate heat from the lattice to the environment. [83, 98, 100–107] However, the time-dependent nanostructure oscillations are convoluted by intra-particle defects, surface morphology, substrate interactions, and neighboring nanostructure interactions. [94, 101, 102, 108–112]

In this work, the goal is to understand the time-dependent structural variations within the gold nanorod lattice and the resulting optical response of the gold nanorod upon absorption of an ultrafast laser pulse. First, the changes in the extinction cross section of gold nanospheres and gold nanorods are simulated using finite difference time domain methods. Upon laser excitation, the generation of breathing and extensional modes results in changes in the size of the nanoparticle and changes in the complex dielectric permittivity of the gold used to model these nanoparticles. To model the combined effects of these changes in physical properties and coupling effects, nanosphere and nanorod dimers are simulated. The second portion of this work explores the time-dependent in-plane lattice displacement within a nanorod assembly on a substrate using finite element methods. The individual effects of substrate adhesion and physical nanoparticle contact is simulated to understand how they affect the lattice displacement.

3.2 Methods

3.2.1 Finite Difference Time Domain Method

The Finite Difference Time Domain (FDTD) method used to determine the extinction cross section is described in Section 2.2.2 on page 11.

3.2.2 Finite Element Method

Finite Element method (FEM) simulations are performed using COMSOL Multiphysics Structural Mechanics and Heat Transfer modules to model the gold nanorod cluster and silicon nitride substrate. FEM subdivides the entire simulation space into a number of finite elements where the equations are modeled in each element then reassembled into the whole simulation space. With this discretization method, the mesh size can be variable across the nanostructure, allowing for a more accurate modeling of curved structures like the nanospheres and nanorods. The in-plane displacement across the nanorod is simulated after the initial temperature increase due to the femtosecond absorption of a laser pulse so both the heat transfer module and structural mechanics module are required. Finally, to account for the substrate interactions, the inclusion of a thin elastic layer is used. This additional layer acts as a spring between the nanorod and the substrate and can be used to model the nonradiative energy loss from the nanorod to the substrate.

3.3 Nanosphere and Nanorod Resonance Shifts with Breathing and Extensional Modes

3.3.1 Changes in the Complex Dielectric Function of Gold upon the Absorption of an Ultrafast Laser Pulse

Upon laser excitation, physical properties of the gold nanostructure change. When the nanoparticle lattice expands, there is a corresponding expansion in the nanoparticle volume. This can be easily modeled by changing the size of the nanoparticle. However, with this change in size, the electron density across the entire nanostructure changes. [113] This affects the complex dielectric permittivity of the nanoparticle, and therefore its resonance. Consider the electron density, N, in the expanded gold nanoparticle. Compared to the initial electron density in the unexpanded nanoparticle:

$$N = \frac{N_0}{1 + \frac{\Delta V}{V_0}} \tag{3.1}$$

where ΔV is the change in volume and V_0 is the initial volume of the unexpanded nanoparticle. The bulk plasmon frequency, ω_p, is a function of electron density:

$$\omega_p = \sqrt{\frac{Ne^2}{\epsilon_0 m}} \sim \sqrt{N} \tag{3.2}$$

where e is the electron charge, m is the mass of the electron, and ϵ_0 is the electric permittivity in vacuum. So the plasmon frequency in the expanded nanoparticle can be determined from the plasmon frequency and electron density of the unexpanded nanoparticle, $\omega_{p,0}$ and N_0, respectively.

$$\omega_p = \omega_{p,0}\sqrt{\frac{N}{N_0}} \tag{3.3}$$

Thus to account for the change in electron density, the new bulk plasmon frequency is used in the Lorentz-Drude oscillator model for the frequency dependent permittivity of gold:

$$\varepsilon_f(\omega) = 1 - \frac{\omega_p^2}{\omega(\omega + i\Gamma)} + \omega_p^2 \sum_{m=1}^{m=\infty} \frac{f_m}{(\omega_{0,m}^2 - \omega^2) - i\omega\Gamma_m} \tag{3.4}$$

where f is the oscillator strength, $\omega_{0,m}$ is the inter-band transition frequencies, and Γ is the linewidth of these transitions. For this work the five oscillator fit is used based on the work of Rakić et. al. [76]

To examine the effects of the change in volume and electron density on the optical response, single and dimer gold nanospheres and gold nanorods are simulated using Lumerical FDTD Solutions. The size and modified complex dielectric permittivity of gold is used to account for the change in optical properties due to volume and electron density, respectively.

3.3.2 Changes in the Extinction Cross Section of Gold Nanospheres upon Laser Excitation

To examine the effect of the absorption of a laser pulse on the resonance modes of gold nanoparticles, the simplest case of the nanosphere is examined. Figure 3.1 shows the extinction cross section of a 60 nm diameter gold nanosphere. For the breathing mode of the nanosphere, the volume expansion to a 61 nm diameter gold nanosphere leads to a small redshift (496 nm to 497 nm) and slight increase in the extinction cross section. Upon inclusion of the decrease in electron density in addition to the volume expansion,

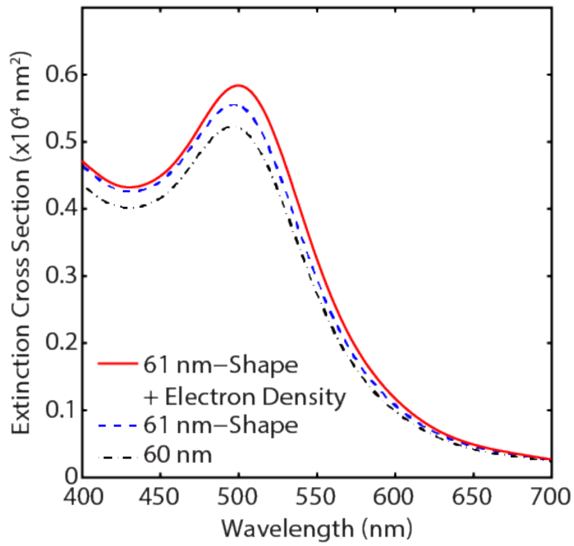

Figure 3.1: Extinction cross sections of the base gold nanosphere (60 nm diameter), the breathing mode of the gold nanosphere with its shape change (61 nm diameter), and the breathing mode of the gold nanosphere with both a shape change and a modified complex dielectric permittivity due to the change in electron density (61 nm diameter + electron density).

the extinction cross section further redshifts (497 nm to 500 nm) and increases compared to the original 60 nm diameter gold nanosphere. Thus for the breathing mode for the nanosphere, the increase in volume and decrease in electron density both redshift and increase the magnitude of the extinction cross section. For this spherically symmetric system, the polarization of incident light does not affect the resonances.

Upon the addition of a second nanosphere, the coupling between the nanospheres as well as the changes in size and electron density of the individual nanospheres are convoluted in the dynamic optical properties of the system. Moreover with the break in spherical symmetry, the polarization of incident light affects the response of the dimer. Thus these dimer systems are simulated with light incident parallel and perpendicular to the dimer axis. Figure 3.2(a) illustrates the extinction cross sections with varying dimer spacing and varying incident polarization for the 60 nm diameter gold nanosphere dimer. With incident

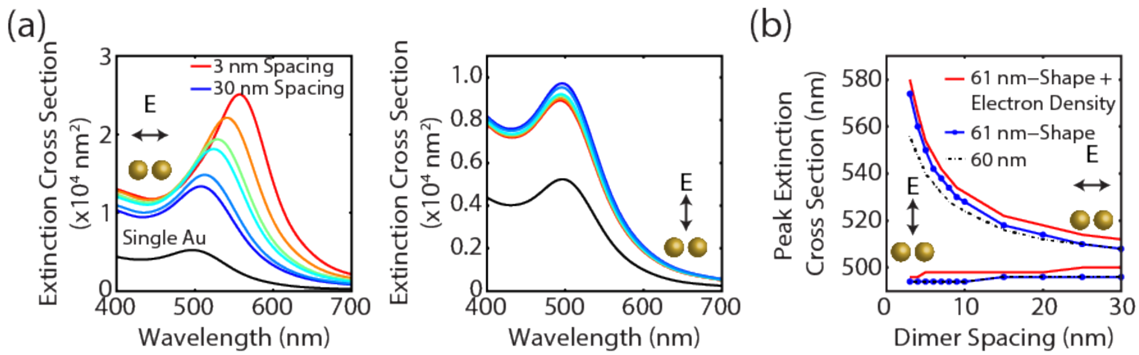

Figure 3.2: Extinction cross sections of the gold nanosphere dimer (60 nm diameter) at varying dimer spacing. (a) Extinction cross sections of the base gold nanosphere dimers with different edge-to-edge spacing for light polarized along the dimer axis and perpendicular to the dimer axis. (b) Variation in the peak extinction cross section wavelength of the dimer system with varying light polarization direction and inclusion of the shape and electric density changes.

polarization along the axis of the dimer, the extinction cross section increases and redshifts significantly with decreasing dimer spacing. For the polarization perpendicular to the dimer axis, there is a much smaller change in peak wavelength of the extinction cross section and a slight decrease in the extinction cross section with decreasing dimer spacing. Figure 3.2(b) examines the variation in peak wavelength of the extinction cross section with dimer spacing. For light polarized perpendicularly to the dimer axis, there is a minimal shift in the peak wavelength with varying dimer spacing, change in size, and change in electron density. When the light is polarized along the axis, a redshift with decreasing particle-to-particle spacing is observed when the size and electron density changes are included. With the increase in size from expansion, the additional redshift arises due to both the larger size of the nanosphere as well as the decrease in dimer edge-to-edge spacing. When accounting for the electron density changes, the resonance further redshifts. The change in dimer spacing results in more significant shifts in the peak extinction cross section compared to the effects of the changing shape and electron density. The impact is largest when the initial dimer spacing is small, since the increased size of the individual nanospheres results in the nanospheres being in closer proximity to one another.

3.3.3 Changes in the Extinction Cross Section of Gold Nanorods upon Laser Excitation

To further investigate the effects of the size and electron density changes on a more complex nanoparticle, gold nanorods are used. Figure 3.3 illustrates the changes in the extinction cross section with the extensional and breathing modes and inclusion of the electron density changes for light polarized along the nanorod axis and perpendicular to the nanorod axis. Starting with 40 nm wide x 120 nm long gold nanorod, the extensional mode is a 39 nm x 121 nm nanorod while the breathing mode is a 41 nm x 119 nm nanorod.

First consider incident light polarized perpendicular to the nanorod axis. The change in shape from the extensional mode slightly decreases the extinction cross section due to the slight decrease in the diameter of the nanorod. The extensional mode results in a four percent decrease in volume, which results in a larger electron density, blueshifting the resonances slightly (480 nm to 478 nm) along with a decrease in the magnitude of the extinction cross section. For the breathing mode, the nanorod is wider in this polarization direction, which results in a slight increase in the magnitude of the extinction cross section. The breathing mode results in a four percent increase in volume, which reduces the electron density in the nanorod, redshifting the resonance slightly (480 nm to 484 nm) along with an increase in the magnitude of the extinction cross section.

For light incident parallel to the axis of the nanorod, the changes in the extinction cross section are more significant. Considering the extensional mode, the increase in nanorod length redshifts the resonance compared to the base nanorod (668 nm to 678 nm) but the larger electron density blueshifts the resonance (678 nm to 671 nm). For the breathing mode,

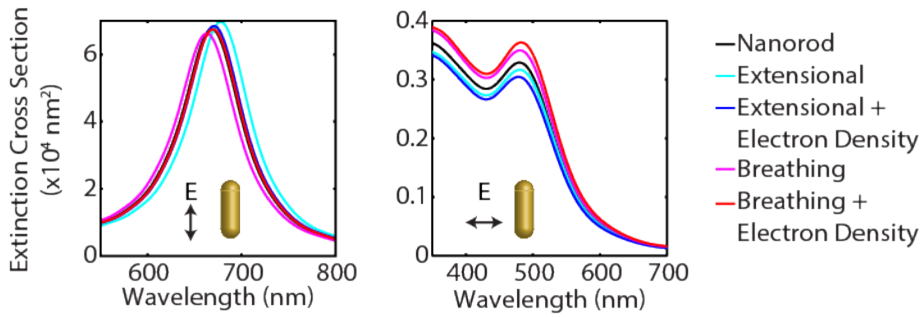

Figure 3.3: Extinction cross sections of the base gold nanorod (40 nm wide x 120 nm long), the extensional mode of the gold nanorod (39 nm wide x 121 nm long), and the breathing mode of the gold nanorod (41 nm wide x 119 nm long), with different incident polarizations and inclusion of the electron density changes.

the decrease in nanorod length blueshifts the resonance compared to the base nanorod (668 nm to 663 nm) but the smaller electron density redshifts the resonance (663 nm to 669 nm). With incident light polarized along the nanorod axis, the size effect and the electron density effect shift the peak extinction cross section wavelength in opposite directions, which is not seen with the nanosphere system.

Similar to the nanosphere dimer, the addition of a second nanorod introduces the coupling effect between the nanorods and convolutes the extinction cross section response of the dimer system. Figure 3.4 shows the extinction cross section for a nanorod dimer pair in the side-by-side arrangement. Similar to the single nanorod case, with light polarized parallel to the nanorod axis, the same competing resonance shift affects of the size and electron density for both the extensional and breathing modes. The addition of the adjacent nanorod blueshifts the extinction cross section compared to the single nanorod system. With increasing dimer spacing, the peak extinction cross section redshifts towards the peak wavelength observed for the single nanorod system as the nanorods in the dimer decrease their interactions with one another.

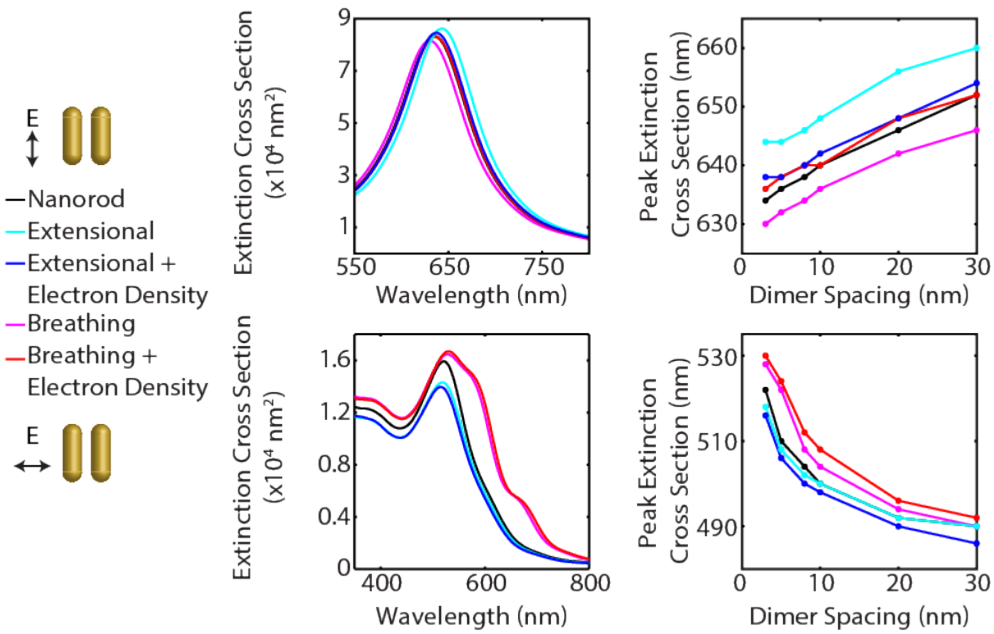

Figure 3.4: Extinction cross sections of the dimer gold nanorods in the side-by-side arrangement. Example extinction cross sections with a three nanometer dimer spacing with different incident polarizations and inclusion of the extensional and breathing modes with and without the corresponding electron density changes. Peak extinction cross section wavelength with varying dimer spacing and inclusion of the extensional and breathing modes with and without the corresponding electron density changes.

For light polarized perpendicular to the nanorod axis, a larger difference in the extinction cross section is seen in the extinction peak for the breathing mode. Again, this is due to the reduced spacing between the nanorods when both nanorods enlarge. The rest of the trends observed for the single nanorod are similar.

Whereas the presence of the adjacent nanorod shifted the peak extinction cross section wavelength in the side-by-side arrangement for both polarizations of incident light, a large shift in peak extinction cross section is observed in the end-to-end arrangement only for light polarized along the axis of the end-to-end dimer arrangement. Figure 3.5 shows the extinction cross section for the nanorod dimer pair in the end-to-end arrangement. Again,

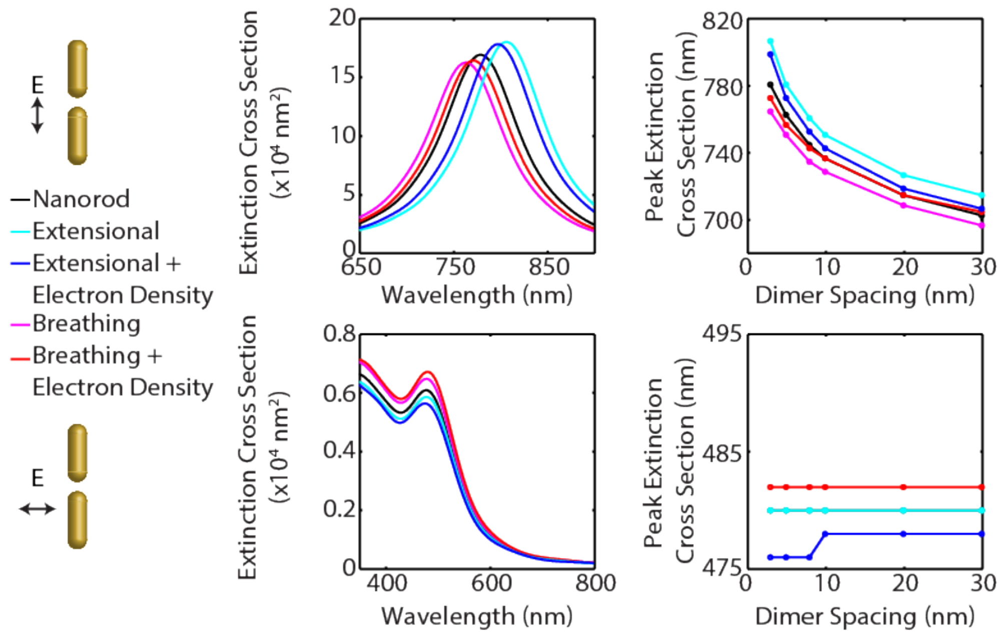

Figure 3.5: Extinction cross sections of the dimer gold nanorods in the end-to-end arrangement. Example extinction cross sections with a three nanometer dimer spacing with different incident polarizations and inclusion of the extensional and breathing modes with and without the corresponding electron density changes. Peak extinction cross section wavelength with varying dimer spacing and inclusion of the extensional and breathing modes with and without the corresponding electron density changes.

the same competing resonance shifts for the shape change and electron density change are seen in this dimer arrangement. For light polarized perpendicular to the axis, there is no change in the peak extinction cross section. When light is polarized parallel to the dimer axis, the nanorod length increase from the extensional mode, along with the reduction in spacing between the particles, redshifts the resonance from 780 nm to 807 nm. Upon inclusion of the change in electron density, the peak resonance blueshifts to 798 nm. For the breathing mode, the slight nanorod length decrease and increase in spacing between the particles blueshifts the peak resonance from 780 nm to 764 nm, and when the change in electron density is included the peak resonance redshifts to 772 nm. These significant shifts indicate the utility of nanorods compared to nanospheres as probes.

3.4 Modeling Contrast Waves Observed in a Gold Nanorod Cluster on Silicon Nitride

3.4.1 Finite Element Model Parameters

Finite element simulations are performed using COMSOL Multiphysics Structural Mechanics and Heat Transfer modules to model the system consisting of four gold nanorods with a 2 nm citrate ligand coating lying on a Si_3N_4 fixed substrate. This system is chosen to replicate the experimental data analyzed by Ryan Gnabasik. The orientation of the nanorods and spacing is taken from a transmission electron microscopy (TEM) image. [98] Each nanorod is modeled as an ideal hemisphere-capped cylinder with radius of 20 nm and total length of 120 nm. The substrate is modeled as a 400 nm x 300 nm x 20 nm block and is fixed on the five surfaces not in contact with the gold nanorods. The heat transfer in solids module provides information regarding thermal expansion and the temperature data is coupled into the linear elastic structural module to model this system over a 100 ps duration after the initial impulse heating due to the absorption of the laser pulse. The pulsed heating is approximated with a 20 K step increase in average temperature in the nanorods determined from thermal diffuse scattering calculations by Ryan Gnabasik. [114–116] Bulk gold and silicon nitride physical properties (elastic moduli, Poisson's ratio, coefficient of thermal expansion, heat capacity at constant pressure, thermal conductivity, and density) are used in the model.

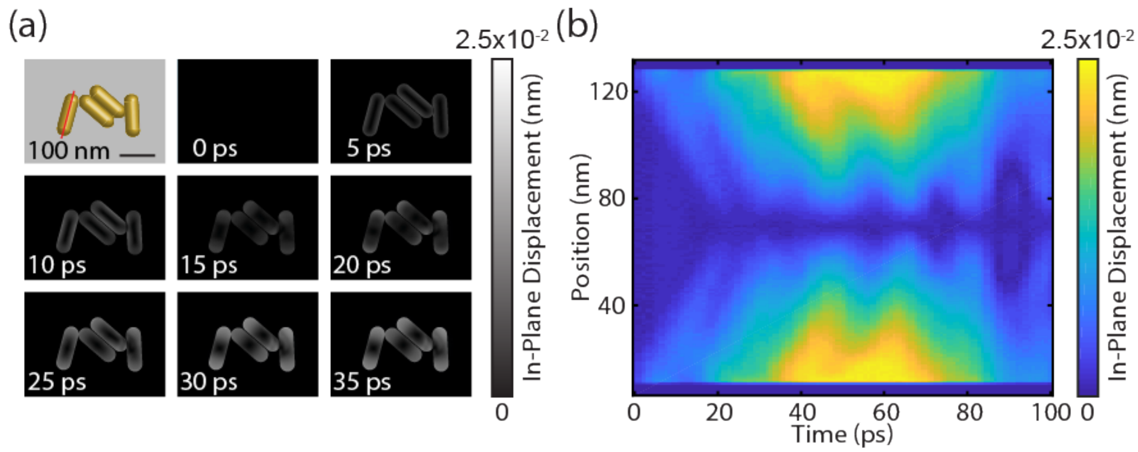

Figure 3.6: Simulated in-plane displacement within the gold nanorod cluster. (a) Top left image is a schematic of the gold nanorod cluster on a silicon nitride substrate modeled in COMSOL. The red line notes the region of interest used to construct the space-time contour plot. A series of images from the in-plane displacement video shows the magnitude of in-plane displacement after an initial isotropic expansion meant to simulate rapid thermal expansion upon ultrafast optical excitation. Black and white denote in-plane displacement from 0 to 25 pm, respectively. (b) Space-time contour plot from the region of interest over the simulated 100 ps. The top and bottom bands with values of zero represent the substrate past the ends of the rods.

3.4.2 Finite Element Simulations of Substrate Effects and Nanorod Interactions on a Gold Nanorod Cluster

The base case simulation results are shown in Figure 3.6 which does not model any contact between the nanorods and does not model any interaction between the nanorods and the silicon nitride substrate. Initially, the increase in in-plane displacement starts at the edges of the nanorods, then collects at the ends of the nanorod before propagating towards the middle. This is seen in all four nanorods in Figure 3.6(a); since the properties of the four nanorods are identical, the time-dependent response from the initial temperature increase is the same.

The generation and propagation of these strain waves may be explained with an analogy to the spring. Upon laser heating, the sudden expansion results in a new equilibrium position. The strain waves allow the lattice to oscillate towards this new equilibrium position. However at later times (beyond 50 ps), the strain waves appear to originate in the middle of the nanorod and propagate towards the ends. This may be due to the interference pattern of the strain wave oscillations colliding in the middle of the nanorod before they begin to oscillate back out towards the ends of the nanorod. A space-time contour plot is created from the left most nanorod of the simulated nanorod cluster, shown in Figure 3.6(b). These strain waves originate at the ends of the nanorod and propagate towards the center in the first 50 ps. The velocity determined from the simulated data is 3.4 nm ps^{-1}, which is close to the bulk speed of sound in gold of 3.24 nm ps^{-1}. [117, 118]

When simulating the structural response, a handful of approximations are taken to simplify the simulation. The nanorods are modeled as ideal hemispherically capped nanorods that are defect free and have isotropic properties. One important property is the Young's modulus, which affects the stiffness of the simulated gold lattice. The Young's modulus for bulk gold is used ($\sim$ 79 GPa). [94, 98] However, in single crystalline nanorods, the Young's modulus is not isotropic and can lead to smaller values in the growth direction [100] along the axis of the nanorod compared to the radial directions (42 GPa in [100] direction vs 81 GPa in [110] direction and 115 GPa in [111] direction). [117, 119] This reduction in Young's modulus will reduce the simulated strain wave propagation velocity, but the in-plane displacement will remain within the nanorods.

Another simplification is the ability to accurately simulate the interaction between the nanorod cluster and substrate. The nanorods can dissipate energy nonradiatively through surface bound ligands, directly into the environment above the nanorod, and directly into the substrate beneath. Figure 3.6(b) shows a symmetric space-time contour plot where the nanorod cluster is in contact with the substrate and does not interact with the substrate. However, realistic nanorod clusters likely interact with the substrate to dissipate energy

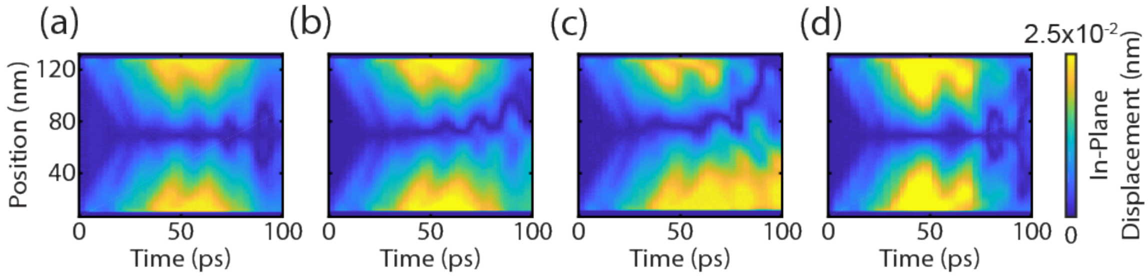

Figure 3.7: Space-time contour plots within the left most nanorod with varying elastic layer coverage. Space-time contour plots showing the in-plane displacement along the red line in Figure 3.6(a) with (a) no elastic layer, (b) elastic layer coverage of the top hemisphere cap, (c) elastic layer coverage of the top third of the nanorod, and (d) elastic layer coverage of all of the nanorod. The elastic layer spring constant is set to 100 GPa and contact is allowed between the nanorods and the substrate.

from the incident laser pulse absorption. Moreover the interactions between the substrate and nanorods may not be uniform along the nanorod, further complicating the simulated in-plane displacement.

To investigate the effect of nonuniform substrate interaction with the nanorod cluster, a thin elastic layer is added between the nanorod and the substrate. This layer has a Young's modulus of 100 GPa to simulate the strength of the coupling between the nanorod and substrate. Varying the Young's modulus from 1 MPa to 50 TPa did not change the simulated results significantly. Figure 3.7 illustrates the space-time contour plots of the left most nanorod in the nanorod cluster with varying coverage of the thin elastic layer. With no elastic layer (Figure 3.7(a)), the middle of the nanorod shows no in-plane displacement over the simulated 100 ps. With just the top hemispheric cap of the nanorod interacting with the substrate (Figure 3.7(b)), the region of no in-plane displacement moves up towards the top of the nanorod with increasing time, breaking the symmetry observed in Figure 3.7(a). This upward shift in the region of zero in-plane displacement is more pronounced when the upper third of the nanorod is interacting with the substrate (Figure 3.7(c)). With increasing substrate interaction at the top of the nanorod relative to the bottom, there is

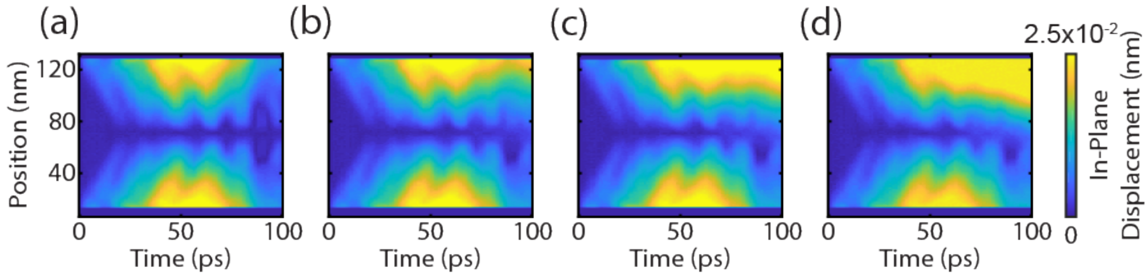

Figure 3.8: Space-time contour plots within the left most nanorod with varying interparticle spacing between the two leftmost nanorods. Space-time contour plots showing the in-place displacement along the red line in Figure 3.6(a). (a)-(d) varies the interparticle spacing between the two nanorods with distances of 0.07, 0.02, 0.00, and -0.03 nm, respectively. These distances correspond to no contact, contact after thermal expansion, initial contact, and initial overlap between the nanorods, respectively. No thin elastic layer is modeled between the nanorods and the substrate for these simulations but contact is allowed between the nanorods and the substrate.

an upward shift of the region of no in-plane displacement. Finally, with the full nanorod interacting with the substrate (Figure 3.7(d)), the space-time contour plot is symmetric again like Figure 3.7(a) when there is no interaction between the nanorod and substrate, but there is a clear difference in the in-plane displacement of the left most nanorod with and without substrate interactions.

Another source of nonradiative energy transfer is through the interactions of nanorods with adjacent nanorods. Again, focusing on the left most nanorod, the top of the left most nanorod is closest in proximity to the nanorod to its right (Figure 3.6(a)). Thus this area is most likely the first part of the nanorod to interact with the neighboring nanorod upon lattice expansion after the absorption of the ultrafast laser pulse. To examine the effects of nanorod contact on the in-plane displacement in the left most nanorod, the initial spacing between the left most nanorod and its neighbor is varied and the resulting space-time contour plots are illustrated in Figure 3.8. With no contact (Figure 3.8(a)), the in-plane displacement is symmetric as seen previously. As the nanorods come in more contact with each other (Figure 3.8(b)-(d)), there is an increase in the in-plane displacement at the top of the left most nanorod. This makes intuitive sense as the interaction with the gold lattice of the neighboring nanorod results in the larger amount of in-plane displacement. Interestingly, this increase in in-plane displacement is isolated to only the top end of the left most nanorod. The bottom half of the nanorod remains mostly the same regardless of the spacing between the left most nanorod and its neighbor. This indicates the localized response of the in-plane displacement to neighboring nanorod contact.

These initial finite element simulations reveal the influence that substrate coupling and proximity to neighboring nanorods has on the simulated in-plane displacement of the nanorod lattice. Non-uniform substrate binding results in the shifting of the region of zero in-plane displacement towards the region of the nanorod with stronger substrate binding. If the nanorods intersect, there is a more localized increase in in-plane displacement within the nanorod. These results isolating the effects of substrate and neighboring nanorods can help deconvolute the more complected responses seen experimentally.

Chapter 4

Upconversion Enhancement using Luminescent Solar Concentrators and Mirrors

4.1 Introduction

Triplet-Triplet Annihilation Upconversion (TTA-UC) is a promising upconversion technique for application in solar cells. [120–127] Unlike other upconversion mechanisms, TTA-UC can occur using noncoherent, weak excitation like sunlight. [123, 127–130] Many highly efficient TTA-UC systems have been studied in the solution phase, but challenges exist in developing solid-state upconverters for device applications. [128, 131–134] One challenge with creating solid-state upconverters is the diffusion of triplets within the matrix, which is limited in viscous environments. Another challenge is the minimization of oxygen, which quenches the excited triplets. [123, 125–127, 135–137]

Recent work by Yanai and Kimizuka has resulted in the development of a simple

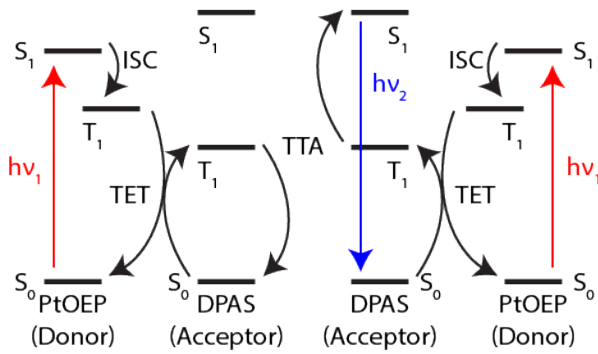

Figure 4.1: Schematic showing triplet-triplet annihilation upconversion pathway for the donor/acceptor PtOEP/DPAS upconverting pair. Energy levels for the singlet states, S, and triplet states, T. Adapted from [127].

and versatile method to create an air-tolerant upconverting hydrogel. [128] The self-assembled hydrogel consists of a gelatin and a nonionic surfactant (Triton-X 100) coassembly encompassing a donor/acceptor upconverting pair, Pt(II) octaethylporphyrin (PtOEP) and sodium 9,10-diphenylanthracene-2-sulfonate (DPAS). The thick, hydrophilic, hydrogen-bonded gelatin shell prevents oxygen from entering the self-assembled hydrogels, minimizing oxygen quenching of the excited triplets generated by the donor and acceptor molecules in the hydrophobic regime. Moreover, the excited triplets can easily diffuse within the coassembly, resulting in a high upconversion efficiency of 13.5%.

Triplet-triplet annihilation is a multi-step photon upconversion process. Figure 4.1 illustrates the upconversion pathway for the donor/acceptor PtOEP/DPAS upconverting pair. First a photon $h\nu_1$ is absorbed by the donor PtOEP molecule and excites a singlet ground state, S_0, to an excited singlet state, S_1. Through intersystem crossing (ISC), the excited singlet state becomes a triplet excited state in the donor PtOEP, T_1. The excited triplet state from the donor PtOEP transfers to an excited triplet state in the acceptor DPAS molecule through triplet energy transfer (TET). When two excited triplet states in two acceptor DPAS molecules are in close proximity, they undergo triplet-triplet

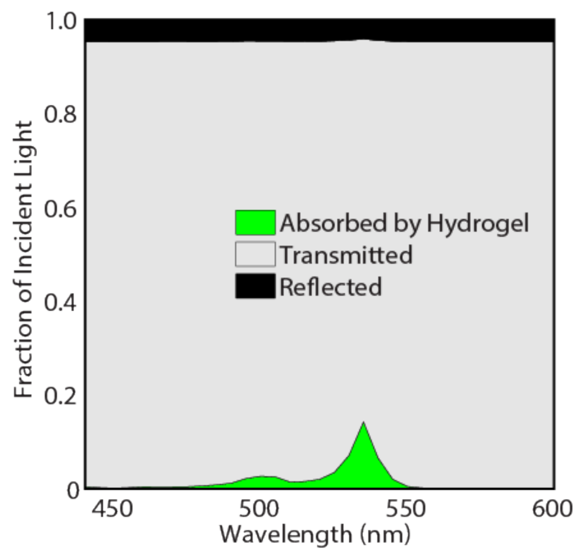

Figure 4.2: Distribution of incident light on the upconverting hydrogel.

annihilation (TTA), resulting a single higher energy singlet state in the acceptor DPAS, S_1. Finally, this excited singlet state relaxes down to the singlet ground state, emitting an upconverted photon $h\nu_2 > h\nu_1$.

One concern with the upconverting hydrogel is the low absorption. Figure 4.2 illustrates the fraction of incident light that is absorbed by the hydrogel, transmitted through the system, or reflected off the hydrogel. The hydrogel absorption accounts for less than one percent of the total fraction of incident light. With the non-unity quantum yield of the upconversion process along with the non-unity quantum yield of the DPAS emitter, the number of upconverted photons is further reduced compared to the number of absorbed photons. This illustrates the need for light management techniques to increase absorption within the hydrogel for increased upconverted PL.

Previous work has examined various light management techniques to increase the flux of light into upconverters. One approach uses plasmonic antennas to enhance upconversion efficiencies [138], while others have examined the use of fluorescent materials to return some of the transmitted light back into the upconverter. [139–142] One promising light concentration technique uses a luminescent solar concentrator (LSC). LSCs embedded with QDs provide geometric concentration by absorbing incident light over a large area and guiding the light through total internal reflection towards a smaller area. QDs are a promising luminophore for this application due to their high quantum yield, tunability, and narrow PL band. In this system, a broad spectral range of incident light is absorbed, and a narrow PL band concentrates light that overlaps the absorption peak of the donor PtOEP molecule. However, LSCs are limited by various loss mechanisms including non-unity quantum yield of the embedded QDs and reabsorption losses that arise from spectral overlap between both the upconverted PL and the QD absorption and the QD PL with its own absorption band. [13, 43, 143–145]

Using an LSC is advantageous, as the LSC absorbs a broad spectrum of incident wavelengths and emits in a narrow PL band that better overlaps with the absorption spectrum of the PtOEP donor. Specular and diffuse mirrors placed beneath the hydrogel can reflect the transmitted light back into the hydrogel to be absorbed, increasing the absorption length and thus the absorption within the hydrogel. In this work, both LSCs and mirrors are used to increase the absorption and subsequent upconverted PL out of the upconverting hydrogel containing the donor/acceptor pair PtOEP/DPAS. Monte Carlo simulations are used to model the propagation of incident light within the system containing the upconverting hydrogel and various light management devices. The benefits of a thin film LSC on a glass slide versus a thick LSC slab for improved upconverted PL is examined as well. This work is done in collaboration with the Yanai and Kimizuka group at Kyushu University.

4.2 Methods

4.2.1 Monte Carlo Algorithm

Monte Carlo models are effective tools to simulate the propagation of photons within luminescent solar concentrators (LSC) when the sizes within the LSC system are much larger than the wavelength of light. The models are based on ray tracing calculations. [29, 30, 40, 145–147] This model is based on home-written code developed by Dr. Ryan Connell. [30] Briefly, the model determines probability functions for the absorption, PL, reflection, and refraction of photons as they interact with the different emitters and layers within the LSC system, as well as the mirrors around the LSC. The user defines the absorption and PL spectral data, optical density of emitters in the layers, quantum yield of the emitters, and geometry of the LSC system, and then the wavelength dependent probability of interaction for a photon is determined in each iteration of the code as the photon propagates through the model in small steps (5 μm). The photon position is tracked throughout the simulation to determine whether it reaches its destination or is lost to various pathways. Thus using hundreds of thousands of photons, the average behavior can be modeled using fewer assumptions than required for analytical models.

To accommodate the upconverting layer, a few modifications are made to the Monte Carlo code developed by Dr. Ryan Connell. A new layer for the upconverting layer is defined, which is positioned either centered on top of the LSC layer or adjacent to the edge of the LSC layer. The absorption and PL properties of the donor and acceptor molecules are entered into the model, along with the relevant optical properties including quantum yield and optical density. The wavelength dependent probability of absorption and PL are calculated similar to the probability of absorption and PL within the LSC. The model approximates the upconversion process as follows. Upon absorption of a photon by the donor molecule in the upconverting layer, a random number from zero to one is generated and compared to the probability of triplet energy transfer to determine whether the photon undergoes triplet energy transfer from the donor to the acceptor molecule. If the photon does not undergo triplet energy transfer, the photon proceeds with the reabsorption and reemission calculations for the donor molecule. After successful triplet energy transfer, another random number is generated to compare to the upconversion quantum yield to determine whether the photon undergoes upconversion or is lost nonradiatively. Upon successful upconversion, the photon is assigned a new wavelength based on the PL spectrum of the acceptor molecule and a random normalized velocity vector to emulate isotropic PL.

One limitation of this upconversion methodology is the tracking of only one photon for this two photon process. Since this Monte Carlo method tracks one photon at a time, there are approximations made when using the probability of triplet energy transfer and upconversion quantum yield. In the case of high intensity illumination, where there is a high density of triplet excited states in the donor molecules, this method of modeling the upconversion process is reasonable since at high illumination intensities beyond the intensity threshold, the upconversion quantum yield is constant. However at low excitation intensities, the constant upconversion quantum yield does not hold since there is not a saturation of triplet excited photons in the donor molecules.

4.2.2 Monte Carlo Parameters

The simulated hydrogel size ranges from a 1 mm x 20 mm x 1 mm slab to 10 mm x 20 mm x 1 mm slab of the upconverting donor/acceptor pair PtOEP/DPAS within the gelatin/TX-100 assembly. The refractive index of the hydrogel is set to 1.37 based on the weighted average (20 wt% gelatin) of the refractive indices of gelatin (1.53) and water (1.33). [148] Based on previous reports, the fluorescent quantum yield of the donor PtOEP (0.40), fluorescent quantum yield of acceptor DPAS (0.667), triplet energy transfer yield between PtOEP and DPAS (0.978), and PtOEP/DPAS upconversion quantum yield (0.135) are used. [128, 149–151] The thick LSC slab is a 10 mm x 40 mm x 1 mm slab of QDs embedded in PLMA. The refractive index of the LSC is set to 1.44, which is the measured index for PLMA. [39] QDs are assumed uniformly distributed within the PLMA with minimal aggregation to ensure high transparency within the LSC. The optical density (OD) at 450 nm in the LSC is fixed to 0.3. The quantum yield of the QDs is fixed at 0.8. For the thin film LSC on glass, the thin film LSC is 10 mm x 40 mm x 50 μm on top of a 10 mm x 40 mm x 950 μm glass slide with a refractive index of 1.50. The specularly reflective and diffusely reflective bottom mirrors with reflectivity of 0.99 are used to increase the absorption length of photons in the system. A 25 μm air gap is set on all sides of the system. The incident photons simulated have wavelengths spanning 440 − 750 nm and are distributed over the top surface. This ensures all the PL from the DPAS upconverter acceptor is light that undergoes upconversion in the hydrogel. The spacing of the incident positions varies across the simulated systems but at least 600,000 photons at each wavelength are simulated over each region (the area over the hydrogel and the area over only the LSC).

4.3 Spectral Overlap Reduces Upconverted PL

The LSC enhances absorption of incident light in the upconverting hydrogel through spectral concentration. Illustrated in Figure 4.3(b), the absorption spectrum of the PtOEP donor molecule consists of a narrow peak around 534 nm. Thus incident light from 440 - 520 nm is unlikely to be absorbed by the PtOEP in the hydrogel. This limits the amount of broadband light absorbed and thereby limits the amount of light upconverted by the hydrogel. To overcome this limit, the LSC with embedded QDs can be used to capture some of this unabsorbed light. The broad absorption spectrum of the QDs in the LSC indicates the QDs strongly absorb the incident light from 440 nm to 520 nm. The resulting PL is centered around 540 nm with a narrow FWHM around 30 nm. This overlaps with

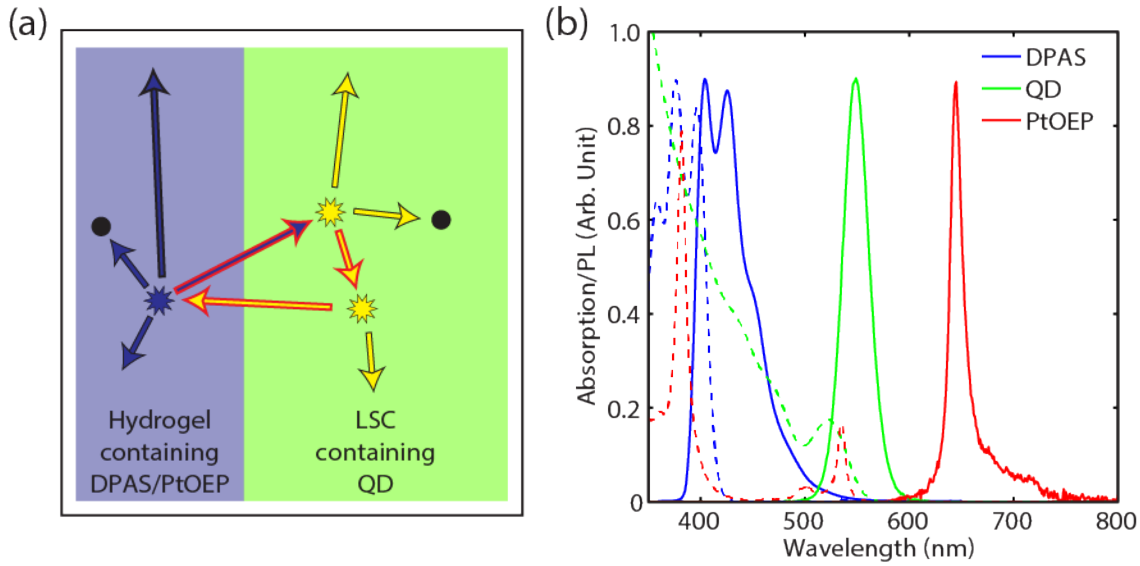

Figure 4.3: Schematic showing the reabsorption loss pathways for upconverted photons in the hydrogel-LSC system due to spectral overlap between the QDs in the LSC and the donor/acceptor upconverting pair PtOEP/DPAS in the hydrogel. (a) Schematic showing the reabsorption loss pathways of upconverted PL from the hydrogel. Blue and yellow stars illustrate PL from the DPAS acceptors and the QDs, respectively. Black dots illustrate non-radiative reabsorption losses due to non-unity quantum yield. Blue and yellow arrows are upconverted PL from the DPAS acceptors and PL from the QDs, respectively. (b) Absorption and PL spectra of DPAS, QD, and PtOEP. Dashed and solid lines are the absorption and PL spectra, respectively.

the narrow PtOEP absorption peak so more of the incident light can be absorbed by the PtOEP donor molecule.

Some reabsorption loss concerns arise when examining the spectral overlap between the upconverted DPAS PL from the hydrogel and the broad QD absorption in the LSC. The spectra shown in Figure 4.3(b) indicate that there is overlap between the DPAS PL and the QD absorption. Since the upconverted photons are emitted isotropically, some of these photons propagate back into the LSC and are reabsorbed by the embedded QDs (Figure 4.3(a)). Due to the non-unity quantum yield of the QDs, some of these upconverted photons are lost nonradiatively, reducing the number of upconverted photons from the hydrogel. The

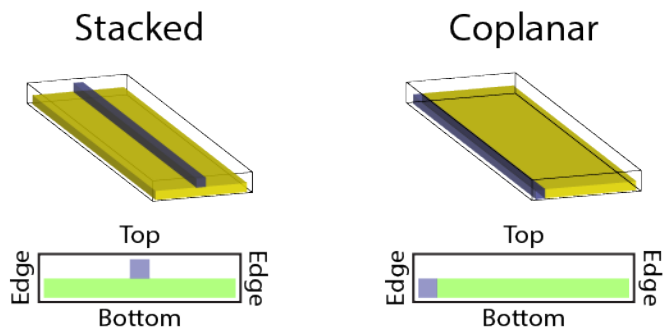

Figure 4.4: Schematic illustrating the two geometric arrangements of the upconverting hydrogel (blue) and the luminescent solar concentrator (yellow). Side profiles of the two schematics are shown below noting the relative proximity of the upconverting hydrogel to the bottom of the simulation.

rest of these formerly upconverted photons are reemitted isotropically and are no longer at the upconverted wavelength. Only a fraction of the reemitted photons propagate through the LSC back into the hydrogel for a chance to be upconverted. The photons can be trapped in this cycle, and with each loop, fewer upconverted photons leave the system. While these reemitted photons propagate in the LSC, there are additional photons lost due to the spectral overlap between the absorption and PL of the QDs. PL from one QD can be absorbed by another QD in the LSC. Some of these photons are nonradiatively lost due to the non-unity quantum yield, while the rest of the photons isotropically emit in the LSC to continue propagating. Thus an additional fraction of upconverted photons are lost while propagating through the LSC.

To quantify the effects of the LSC, two different geometries were modeled: the UC hydrogel position may be centered on top of the LSC in the stacked arrangement, or on the side of the LSC in the coplanar arrangement as illustrated in Figure 4.4. An air gap surrounds all sides of the system to ensure efficient light trapping for light propagation within the LSC. Another technique to increase absorption is the use of a mirror on the bottom of the system. Light that is transmitted through both the hydrogel and LSC is reflected back up for a second pass, increasing the absorption path length, and resulting in an increase in absorption and PL from the upconverting hydrogel. Both specular and diffuse mirrors are examined, and are tested in conjunction with the LSC to determine the best combination of light management techniques to increase both the absorption and upconverted PL of the upconverting hydrogel.

4.4 Absorption and PL Enhancement with LSCs and Mirrors

The absorption spectra of the various geometries including the LSC and mirrors is shown in Figure 4.5(a) for a hydrogel size of 1 mm x 40 mm x 1 mm. The best light management strategy for absorption enhancement uses the LSC and a diffuse mirror for both the stacked and coplanar arrangements. To compare the total number of photons absorbed, the sum of the product of the absorption spectrum and the solar spectrum is used to determine the absorption enhancement factor compared to the hydrogel only system for each hydrogel arrangement (stacked or coplanar) (Figure 4.5(b)). Incorporating the LSC and diffuse mirror in the stacked arrangement enhances absorption by a factor of 3.54, while the same system in the coplanar arrangement achieves a factor of 3.72.

When only using just one light management device (the LSC, a diffuse mirror, or a specular mirror), the diffuse mirror provides the largest absorption enhancement within the hydrogel. The diffuse mirror alone enhances absorption by a factor of 2.94 in the stacked arrangement and 2.69 in the coplanar arrangement. The specular mirror increases absorption in both geometries identically. The light transmitted in the first pass is reflected straight back up into the hydrogel to be absorbed in the second pass, resulting in a near 100% increase in absorption with the specular mirror compared to the hydrogel only system.

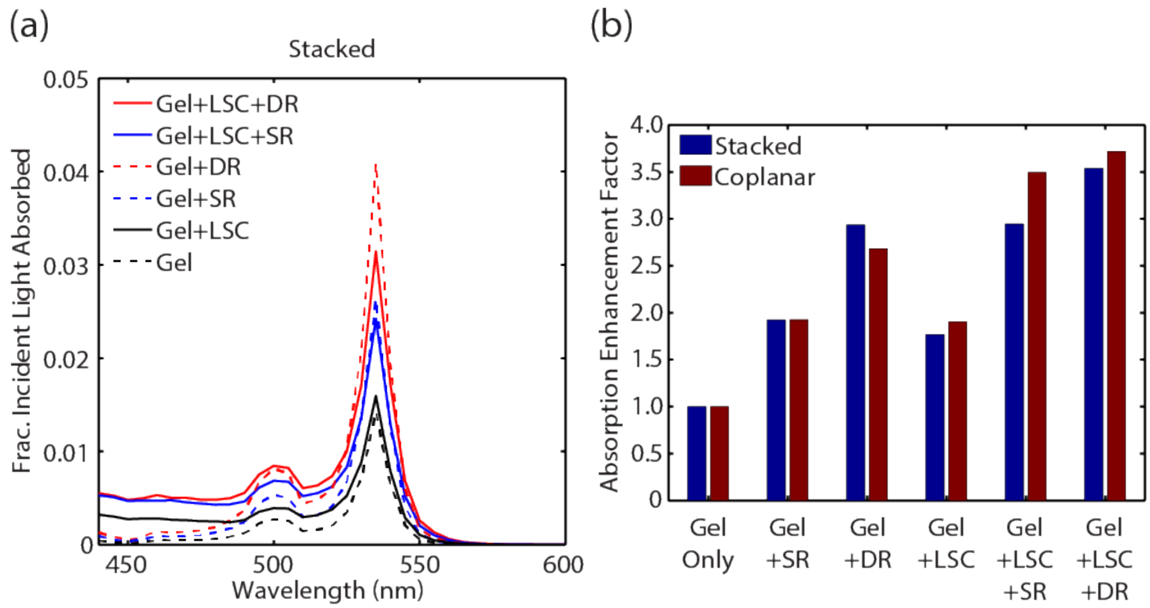

Figure 4.5: Comparison of the absorption within the upconverting hydrogel upon the addition of LSCs and mirrors. (a) Fraction of incident light absorbed in the upconverting hydrogel for the stacked geometries, inclusion of the LSC, and addition of the bottom mirror (specular reflection, SR, and diffuse reflection, DR). (b) Comparison between the incident light absorbed between the stacked and coplanar geometries, inclusion of the LSC, and addition of the bottom mirror. Absorption enhancement factors normalized to the amount of incident light absorbed by the gel only sample.

With the diffuse mirror, incident light is scattered with equal radiance to all angles, so light incident far from the hydrogel can scatter towards the hydrogel to be absorbed. This results in the improved absorption enhancement with the diffuse mirror versus the specular mirror.

Additionally, the central and higher placement of the hydrogel in the stacked arrangement compared to the coplanar arrangement results in greater absorption enhancement with the diffuse mirror. More photons are diffusely reflected into the stacked arrangement since there is a wider range of scattering angles that are directed to the hydrogel than in the coplanar arrangement, as illustrated in Figure 4.4.

With the inclusion of the LSC alone, there is an increase in the absorption enhancement factor compared to the hydrogel only system, but the mirrors provide greater absorption enhancement. With the LSC alone, the increase in photons absorbed derives from photons with wavelengths shorter than 520 nm, whereas with the use of mirrors, the absorption spectrum is just a scalar multiple of the hydrogel only absorption spectrum as illustrated in Figure 4.5(a).

When combining either mirror with the LSC, the absorption enhancement factors are larger than the systems with only one light management device. However this benefit is not additive due to the spectral overlap. Again, examining the fraction of light absorbed in the stacked arrangement with the diffuse reflector in Figure 4.5(a), adding the LSC decreases the fraction of light absorbed around 534 nm. This arises from the slightly higher refractive index in the LSC compared to the upconverting hydrogel (1.44 vs 1.37, respectively). For light that is transmitted in the first pass through the hydrogel and LSC and reflected by the mirror, as it propagates back towards the LSC and hydrogel it first encounters the air/LSC interface. Since the difference in the refractive index between air and the LSC is larger than the different in the refractive index between air and the upconverting hydrogel, a larger fraction of light is reflected off this interface and does not propagate into the LSC or hydrogel to be absorbed. Nonetheless, the combined mirror and LSC system does show improvement over the mirrors alone due to the broad absorption within the LSC, PL from the LSC, and subsequent absorption in the hydrogel.

Although an increase in absorption in the upconverting hydrogel leads to an increase in the number of upconverted photons emitted from the donor/acceptor pairs in the hydrogel, not all of the upconverted PL leaves the simulated system at the upconverted wavelength due to the spectral overlap between the upconverted DPAS PL and the absorption spectrum of the QDs in the LSC. Thus, it is equally important to track the change in the fraction of incident photons that are emitted by the upconverter and the resulting PL wavelength of these photons as they exit the simulated system. As discussed previously, the overlap

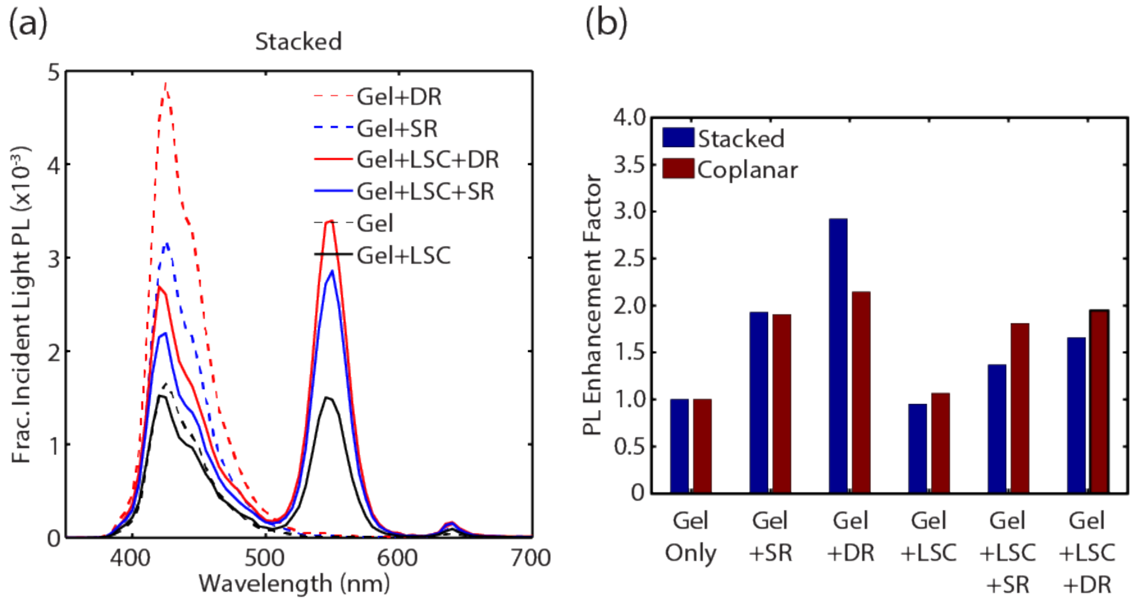

Figure 4.6: Comparison of the PL from the upconverting hydrogel upon the addition of LSCs and mirrors. (a) Fraction of incident light PL from the upconverting hydrogel for the stacked geometries, inclusion of the LSC, and addition of the bottom mirror (specular reflection, SR, and diffuse reflection, DR). (b) Comparison between the number of upconverted PL photons between the stacked and coplanar geometries, inclusion of the LSC, and addition of the bottom mirror. PL enhancement factors normalized to the amount of incident light upconverted and PL by the gel only sample.

between the upconverted DPAS PL spectrum with the absorption spectra of both DPAS and QDs, as well as the absorption/PL spectral overlap for the QDs alone, reduces the number of upconverted photons emitted from the system. The PL spectra for the various geometric arrangements are shown in Figure 4.6. To compare the number of upconverted photons emitted, only the photons with wavelengths shorter than 515 nm are compared to the number of upconverted photons from the hydrogel only system. The best arrangement is the inclusion of only a diffuse mirror in both arrangements, which provides PL enhancement factors of 2.92 and 2.14 for the stacked and coplanar arrangements, respectively. With the inclusion of only the specular mirror, PL enhancement factors of 1.93 and 1.91 are seen compared to the no mirror case. The same reasoning from the absorption enhancement with the specular mirror can be applied to the PL enhancement seen here, as noted by the similar absorption enhancement factor.

With the addition of only a diffuse mirror, the stacked arrangement exhibits a larger PL enhancement factor than the coplanar arrangement due to the increased distance from the bottom of the hydrogel to the bottom mirror. In the coplanar arrangement, only the 25 μm air gap separates the bottom mirror from the hydrogel, so much of the PL light from the hydrogel that scatters diffusely off the bottom mirror reenters the hydrogel to be reabsorbed due to the spectral overlap between the absorption and PL from the DPAS. Due to the low DPAS QY (0.667), many photons are lost nonradiatively upon reabsorption. To prevent the upconverted photon from reentering the hydrogel with such a small gap space between the bottom of the hydrogel and the diffuse mirror, the scattering angle off the bottom mirror must have a large angle relative to the normal of the bottom mirror. This constitutes a small fraction of all possible scattering angles, so a majority of the diffusely scattered upconverted light reenters the hydrogel to be lost nonradiatively. In the stacked arrangement, there is a 1 mm space in addition to the 25 μm air gap to account for the LSC position. This additional vertical space allows for a less restrictive scattering angle relative to the normal of the diffusely scattering bottom mirror to ensure the diffusely scattered upconverted photons do not reenter the hydrogel, resulting in the larger increase in upconverted PL compared to the coplanar arrangement.

With the addition of just the LSC, there is a slight decrease in the number of upconverted photons that leave the system in the stacked arrangement, and a slight increase in the coplanar arrangement with no mirror. The decrease can be explained by the relative position of the hydrogel and LSC. Since half of the isotropically upconverted photons propagate towards the LSC, there is a larger fraction of upconverted photons that pass through the LSC to be reabsorbed and lost via the nonunity quantum yield of the LSC. In the coplanar arrangement a smaller fraction of the isotropically upconverted PL propagates toward the LSC, so fewer photons are lost to reabsorption in the LSC.

However when adding the LSC to the systems with mirrors, there is a reduction in the PL enhancement factor in all cases. This is clearly seen in Figure 4.6(a) with the reduction in the upconverted photons and corresponing increase in QD PL upon inclusion of the LSC. The stacked arrangement has a larger decrease in the PL enhancement factor upon addition of the LSC compared to the coplanar arrangement due to the geometry argument presented earlier. The inclusion of the bottom mirror magnifies these losses by providing additional rebasorption loss pathways in both geometric arrangements, but since the coplanar arrangements has fewer loss pathways, the losses in upconverted PL is less drastic compared to the stacked arrangement.

Finally, to compare the effect of the relative size of the upconverting hydrogel on absorption and upconverted PL enhancement, the absorption and PL enhancement factors are determined for various hydrogel sizes. Figures 4.7 and 4.8 compare absorbed photons and upconverted PL for the stacked arrangement and coplanar arrangement, respectively. Overall the same trends seen for the smallest 1 mm x 40 mm upconverting hydrogel size described previously hold true for the larger sizes.

There is a decrease in both absorption and PL enhancement with increasing hydrogel size in the stacked arrangement, as shown in Figure 4.7. With the larger hydrogel on top of the LSC, there is a larger interface area between the hydrogel and LSC, so there is less of a benefit from geometric concentration to improve absorption in the hydrogel. Furthermore, the larger interface area allows more upconverted light to enter the LSC to be lost through reabsorption and downshifted reemission, which accounts for the reduction in the upconverted PL enhancement factor with increasing hydrogel size. Finally, with increasing hydrogel size, there is less of a difference in the effect of the specular mirror and diffuse mirror, as the hydrogel covers a larger fraction of the entire simulated area

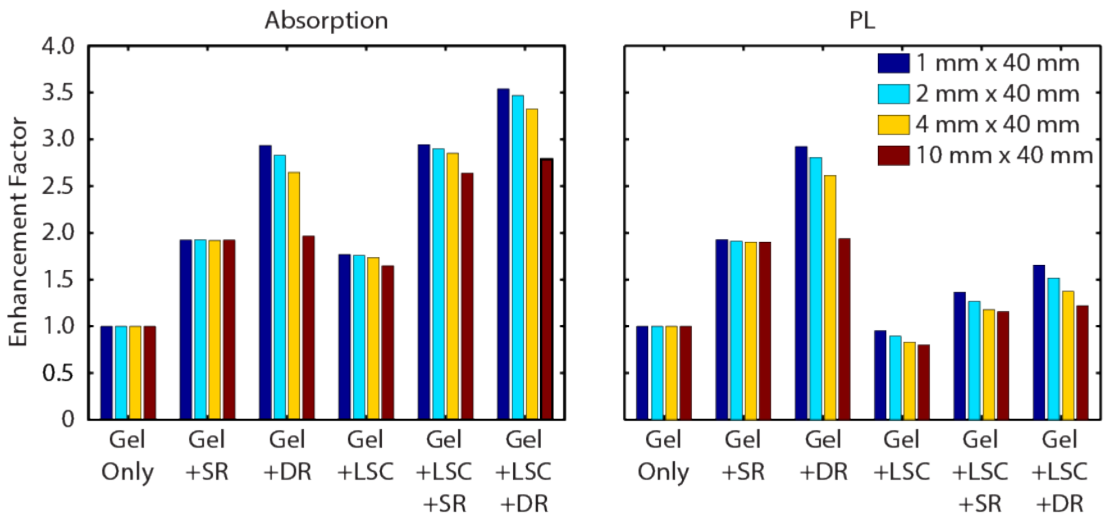

Figure 4.7: Comparison of the number of absorbed photons and upconverted PL for the stacked geometry system with varying upconverting hydrogel size at a fixed 10 mm x 40 mm LSC size, inclusion of the LSC, and addition of the bottom mirror (specular reflection, SR, and diffuse reflection, DR). The legend lists the four sizes of upconverting hydrogel examined.

(from 10% for the 1 mm x 40 mm hydrogel to 100% for the 10 mm x 40 mm hydrogel). At larger hydrogel sizes, there is a smaller fraction of light that passes through air and not the hydrogel and can be diffusely scattered into the hydrogel to be absorbed, thus the enhancement from the diffuse mirror approaches that of the specular mirror with a larger hydrogel in the stacked arrangement. At the largest hydrogel size, all incident light passes through the hydrogel in the first pass, so the increase in absorbed photons for the diffuse mirror and specular mirror are nearly identical.

In the coplanar arrangement, there is a decrease in the absorption enhancement with increasing size upon inclusion of the LSC, as shown in Figure 4.8. Only the region of the hydrogel closest to the LSC absorbs the increased photon flux from the LSC. For larger hydrogel sizes, the regions of the hydrogel away from the LSC do not benefit from the increased photon flux and absorb fewer photons. When averaging over the entire hydrogel,

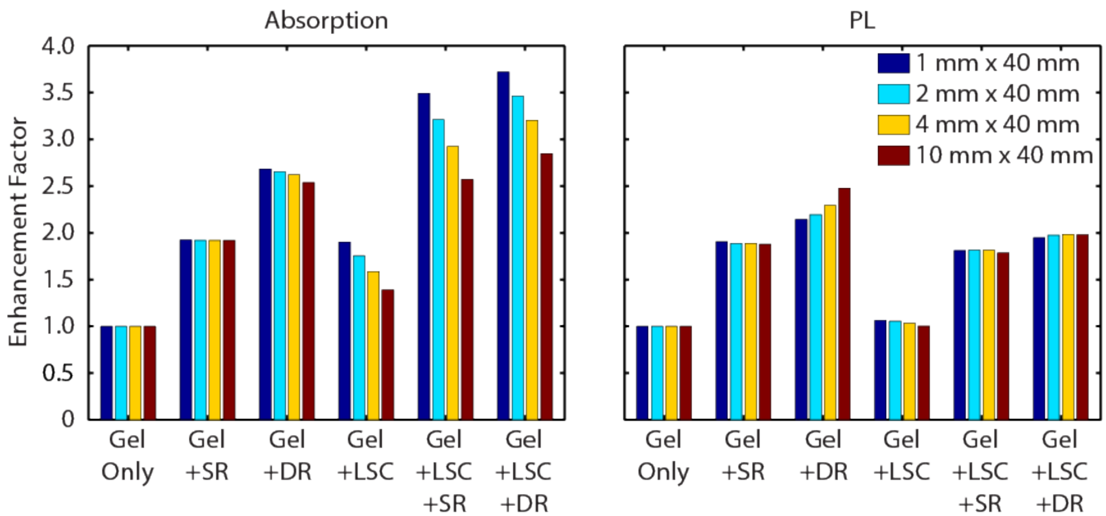

Figure 4.8: Comparison of the number of absorbed photons and upconverted PL for the coplanar geometry system with varying upconverting hydrogel size at the fixed 10 mm x 40 mm LSC size, inclusion of the LSC, and addition of the bottom mirror (specular reflection (SR) and diffuse reflection (DR)). The legend lists the four sizes of upconverting hydrogel examined.

there is less total absorption enhancement since a larger fraction of the hydrogel does not benefit from the additional photons from the LSC. For the upconverted PL enhancement in the coplanar arrangement with the LSC, there is little variation with increasing hydrogel size. There is less upconverted PL reabsorption by the LSC since the interface area between the hydrogel and LSC remains constant. Thus the coplanar arrangement with the LSC results in more PL enhancement than the stacked arrangement with LSC.

For most arrangements shown, increasing the hydrogel size results in a decrease in absorption and PL enhancement. However, the upconverted PL from the coplanar system with only a diffuse reflector shows an increase in PL enhancement with increasing size. This is due to the increasing fraction of the total area occupied by the hydrogel. In the smallest case, the 1 mm x 40 mm hydrogel accounts for 1/11 of the simulated region since the 10 mm x 40 mm LSC accounts for the rest of the area. In the largest case, the 10 mm x 40

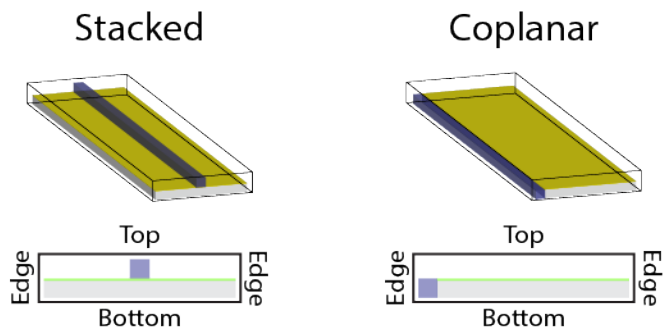

Figure 4.9: Schematic illustrating the two geometric arrangements of the upconverting hydrogel (blue) and the thin film luminescent solar concentrator (yellow) on top of a glass slide. Side profiles of the two schematics are shown below.

mm hydrogel accounts for half of the simulated region. With the larger hydrogel, a larger fraction of diffusely scattered light that doesn't pass through the hydrogel in the first pass is scattered towards the hydrogel to be absorbed and upconverted, resulting in the increase in upconversion PL observed.

In all of the systems examined, there is no upconverted PL enhancement upon addition of the thick LSC slab. This is due to the reabsorption of upconverted light in the LSC layer. To overcome this problem, one alternative is to use a thin QD-polymer layer ($<$ 100 μm) on top of a glass slide. [152, 153] Figure 4.9 illustrates schematics of the different geometries with the thin film on glass. The thin film LSC still absorbs the incident light, but the PL can propagate in the underlying glass layer, free from reabsoprtion loss. Moreover, the upconverted PL from the upconverting hydrogel, when propagating back into the thin film LSC and glass slide, is not absorbed in the glass layer as it propagates, increasing the number of upconverted photons that leave the system.

To model the thin film LSC, the geometry of the simulation is modified again to accommodate the glass slide regime. Instead of having the thick 1000 μm of the LSC region as absorbing LSC, the thin film LSC consists of a 50 μm thin film LSC on top of a 950 μm glass slide. Two thin film systems ODs are examined: one with the same OD

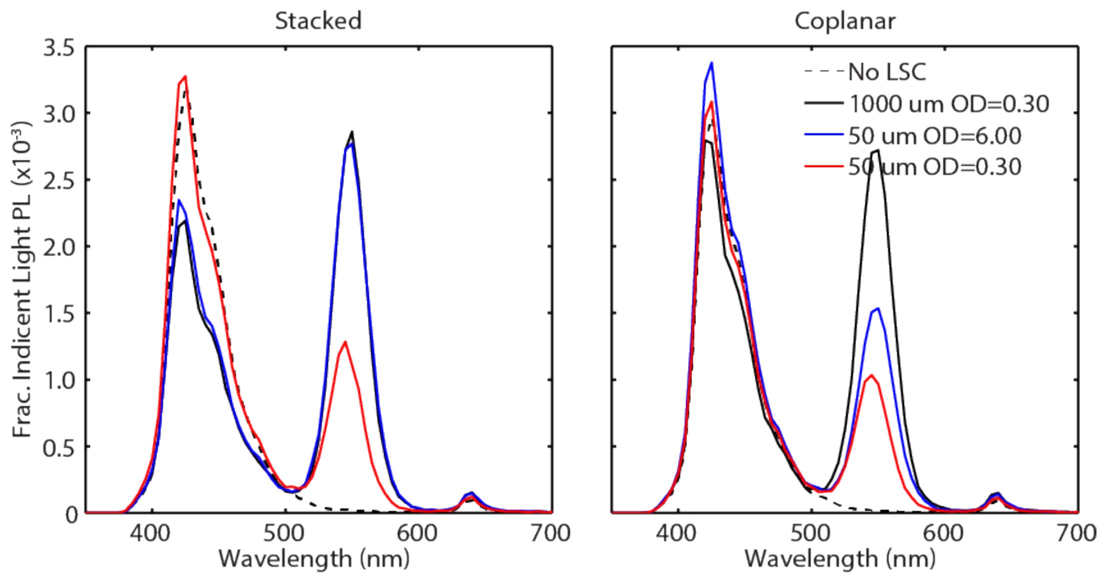

Figure 4.10: Fraction of incident light PL from the upconverting hydrogel with a specular mirror comparing the thin film LSC and the thick LSC slab.

as the thick film (OD = 0.30) and one with a higher OD to compensate for the reduced thickness (OD = 6.00). Only the PL enhancement for the smallest upconverting hydrogel is simulated to determine whether the thin film LSC is more advantageous than the thick LSC slab.

Figure 4.10 illustrates the PL spectra comparing the different LSCs for both the stacked and coplanar arrangement. With the thin film LSC on the glass slide, PL enhancement is achieved with the addition of the thin film LSC in the coplanar arrangement. In the stacked arrangement, no PL enhancement is observed. With the thin film LSC with high OD, the PL spectrum is similar to that of the thick LSC slab, whereas with the thin film LSC with low OD, the PL spectrum is similar to the system with no LSC except for the addition of PL peaks from the QDs and PL from the PtOEP that is not upconverted. In the stacked arrangement, the same geometric problem exists in this thin film LSC system as discussed above for the thick LSC slab system. Since all of the upconverted PL emitted down again must pass through the LSC, there is the same reduction due to reabsorption and subsequent losses in the LSC. This is less of a concern with the lower OD thin film LSC, but no PL enhancement is observed. On the other hand in the coplanar arrangement, there is upconverted PL enhancement. With the upconverting hydrogel on the side of the thin film LSC and glass slide assembly, most of the upconverted light propagating towards the thin film LSC/glass side can travel undisturbed through the glass slide. Similarly, the light absorbed by the thin film LSC is emitted and propagates through the glass slide towards the upconverting hydrogel without being reabsorbed, increasing the number of photons that are upconverted. This results in the increase in upconverted PL out of the system seen in Figure 4.10 with the two thin film arrangements. Moreover with the higher OD thin film, more total photons are emitted, as noted by the increase in both the upconverted DPAS PL and the QD PL peaks.

From these Monte Carlo simulations, the interactions of light management devices including the thick LSC slab, thin film LSC on glass, specular mirror, and diffuse mirror are examined to understand how to increase the absorption resulting upconverted PL from the hydrogel. Both the addition of the bottom mirrors and a thick LSC slab increase the absorption within the upconverting hydrogel due to the increased absorption path length and spectral concentration effects. The use of the mirror in both geometric arrangements increases the upconverted PL due to the increased absorption. The thin film LSC on glass increases the upconverted PL only in the coplanar arrangement due to reduction in reabsorption of upconverted PL as it propagates losslessly through the glass.

Chapter 5

Future Work

5.1 Absorption and PL Enhancement of Patterned Quantum Dot Solids using Nanoring Assemblies

Much of the simulated work looking at patterned QD solids in nanophotonic environment explored absorption enhancement around 405 nm. The larger nanoassemblies examined were chosen to examine larger area electromagnetic field enhancement, and were not tuned to be resonant around 405 nm. Future work can examine smaller, aluminum nanorings more closely tuned to 405 nm.

Another direction for future work is to examine PL enhancement around 630 nm. The nanoassemblies can be tuned to be resonant around 630 nm to help outcouple the PL out of the QD solids. These rings are larger and thicker than those tuned for absorption enhancement around 405 nm. Moreover, other plasmonic metals such as gold and silver can be used in this redder region of the wavelength spectrum.

Another option is to use nanoellipses tuned to two different wavelengths. [154] By varying the major and minor axes of the ellipse, two different resonant wavelengths can tuned to simultaneously target the absorption enhancement around 405 nm and PL enhancement around 630 nm. The results from the nanoellipse work can be compared to the nanoring results on the enhancement of absorption and PL.

5.2 Modeling the Response of a Gold Nanorod Cluster Following Ultrafast Laser Illumination

One effect not accounted for in the changes in complex dielectric function upon laser pulse absorption is the deformation potential from the strain in the lattice due to the changing volume, as discussed in recent literature. [113] Recall the Lorentz-Drude oscillator model (Equation 3.4 on page 42). The increase in size causes lattice strain, which affects the band structure within the nanoparticle. This shift in the band energy $\delta E_{0,m}$ can be approximated as:

$$\delta E_{0,m} = \xi_m \frac{\delta V}{V} \tag{5.1}$$

where ξ_m is the deformation potential and the fractional change in volume can approximate the strain. This causes shifts in the oscillator frequencies, $\omega_{0,m}$, which is approximated as:

$$\omega_{0,m}^{new}(r) = \omega_{0,m} + \frac{\delta E_{0,m}}{\hbar} = \omega_{0,m} + \frac{\xi_m}{\hbar}\frac{\delta V}{V} \tag{5.2}$$

Finally, this new spatial dependent oscillator frequency can be integrated over the volume of the nanosphere to determine the permittivity of the gold while accounting for the strain in the lattice. This requires determination of the deformation potential for the five oscillator frequencies in Lorentz-Drude model used in this work.

5.3 Upconversion Enhancement using Luminescent Solar Concentrators and Mirrors

With the thin film LSC system, different thin film LSC thicknesses and optical densities can be examined to maximize the upconverted PL from the upconverting hydrogel by balancing the increased absorption of incident light and the spectral concentration of light onto the hydrogel against the reabsorption of upconverted PL in the LSC.

Another method to improve both the thick LSC slab and thin film LSC systems is the use of a long pass mirror to prevent upconverted light from entering the LSC. By placing a long pass mirror between the upconverting hydrogel and LSC, the reabsorption of upconverted PL by the LSC can be reduced. This prevents the upconverted PL from entering the LSC while letting the longer wavelength, spectrally concentrated PL from the QDs in the LSC enter the hydrogel. By limiting one pathway for reabsorption losses of upconverted PL, the resulting upconverted PL can be increased further to achieve higher PL enhancement factors.

Bibliography

[1] S. V. Gaponenko, *Introduction to nanophotonics* (Cambridge University Press, 2010).

[2] S. A. Maier and H. A. Atwater, "Plasmonics: localization and guiding of electromagnetic energy in metal/dielectric structures", Journal of Applied Physics **98**, 011101 (2005).

[3] A. Polman and H. A. Atwater, "Photonic design principles for ultrahigh-efficiency photovoltaics", Nat Mater **11**, 174–177 (2012).

[4] W. E. I. Sha, H. L. Zhu, L. Chen, W. C. Chew, and W. C. H. Choy, "A general design rule to manipulate photocarrier transport path in solar cells and its realization by the plasmonic-electrical effect", Scientific Reports **5** (2015).

[5] S. A. Maier, *Plasmonics: fundamentals and applications* (Springer US, 2007).

[6] V. Giannini, A. I. Fernández-Domínguez, S. C. Heck, and S. A. Maier, "Plasmonic nanoantennas: fundamentals and their use in controlling the radiative properties of nanoemitters", Chemical Reviews **111**, 3888–3912 (2011).

[7] J. A. Schuller, E. S. Barnard, W. Cai, Y. C. Jun, J. S. White, and M. L. Brongersma, "Plasmonics for extreme light concentration and manipulation", Nat. Mater. **9**, 193–204 (2010).

[8] K. A. Willets and R. P. Van Duyne, "Localized surface plasmon resonance spectroscopy and sensing", Annual Review of Physical Chemistry **58**, 267–297 (2007).

[9] I. Zorić, M. Zäch, B. Kasemo, and C. Langhammer, "Gold, plasnium, and aluminum nanodisk plasmons: material independence, subradiance, and damping mechanism", ACS Nano **5**, 2535–2546 (2011).

[10] Y. Babayan, J. M. McMahon, S. Li, S. K. Gray, G. C. Schatz, and T. W. Odom, "Confining standing waves in optical corrals", ACS Nano **3**, 615–620 (2009).

[11] M. W. Knight, N. S. King, L. Liu, H. O. Everitt, P. Nordlander, and N. J. Halas, "Aluminum for plasmonics", ACS Nano **8**, 834–840 (2014).

[12] A. Boltasseva and V. M. Shalaev, "All that glitters need not be gold", Science **347**, 1308–1310 (2015).

[13] M. G. Debije and P. P. C. Verbunt, "Thirty years of luminescent solar concentrator research: solar energy for the built environment", Advanced Energy Materials **2**, 12–35 (2012).

[14] Y. Shirasaki, G. J. Supran, M. G. Bawendi, and V. Bulović, "Emergence of colloidal quantum-dot light-emitting technologies", Nature Photonics **7**, 13–23 (2013).

[15] J. R. Lakowicz, *Principles of fluorescence spectroscopy*, 3rd (Springer, 2006).

[16] A. P. Alivisatos, "Semiconductor clusters, nanocrystals, and quantum dots", Science **271**, 933–937 (1996).

[17] P. Würfel, *Physics of solar cells*, 2nd (Wiley-VCH, 2009).

[18] I. Pelant and J. Valenta, *Luminescence spectroscopy of semiconductors*, 1st (Oxford University Press, 2012).

[19] I. Pelant and J. Valenta, *Luminescence spectroscopy of semiconductors*, 1st (Oxford University Press, 2012).

[20] O. Chen, J. Zhao, V. P. Chauhan, J. Cui, C. Wong, D. K. Harris, H. Wei, H.-S. Han, D. Fukumura, R. K. Jain, and M. G. Bawendi, "Compact high-quality cdse–cds core–shell nanocrystals with narrow emission linewidths and suppressed blinking", Nature Materials **12**, 445–451 (2013).

[21] L. Tan, Y. Zhou, F. Ren, D. Benetti, F. Yang, H. Zhao, F. Rosei, M. Chaker, and D. Ma, "Ultrasmall pbs quantum dots: a facile and greener synthetic route and their high performance in luminescent solar concentrators", J. Mater. Chem. A **5**, 10250–10260 (2017).

[22] D. A. Hanifi, N. D. Bronstein, B. A. Koscher, Z. Nett, J. K. Swabeck, K. Takano, A. M. Schwartzberg, L. Maserati, K. Vandewal, Y. van de Burgt, A. Salleo, and A. P. Alivisatos, "Redefining near-unity luminescence in quantum dots with photothermal threshold quantum yield", Science **363**, 1199–1202 (2019).

[23] S. Kim, B. Fisher, H.-J. Eisler, and M. Bawendi, "Type-ii quantum dots: cdte/cdse(core/shell) and cdse/znte(core/shell) heterostructures", Journal of the American Chemical Society **125**, 11466–11467 (2003).

[24] Z. A. Peng and X. Peng, "Formation of high-quality cdte, cdse, and cds nanocrystals using cdo as precursor", Journal of the American Chemical Society **123**, 183–184 (2001).

[25] M. Brumer, A. Kigel, L. Amirav, A. Sashchiuk, O. Solomesch, N. Tessler, and E. Lifshitz, "Pbse/pbs and pbse/pbsexs1–x core/shell nanocrystals", Advanced Functional Materials **15**, 1111–1116 (2005).

[26] P. Reiss, M. Protière, and L. Li, "Core/shell semiconductor nanocrystals", Small **5**, 154–168 (2009).

[27] G. Schlegel, J. Bohnenberger, I. Potapova, and A. Mews, "Fluorescence decay time of single semiconductor nanocrystals", Phys. Rev. Lett. **88**, 137401 (2002).

[28] J. I. Pankove, *Optical processes in semiconductors*, 1st (Dover Publications, Inc., 1971).

[29] N. D. Bronstein, L. Li, L. Xu, Y. Yao, V. E. Ferry, A. P. Alivisatos, and R. G. Nuzzo, "Luminescent solar concentration with semiconductor nanorods and transfer-printed micro-silicon solar cells", ACS Nano **8**, 44–53 (2014).

[30] R. Connell and V. E. Ferry, "Integrating photonics with luminescent solar concentrators: optical transport in the presence of photonic mirrors", The Journal of Physical Chemistry C **120**, 20991–20997 (2016).

[31] W. H. Weber and J. Lambe, "Luminescent greenhouse collector for solar radiation", Appl. Opt. **15**, 2299–2300 (1976).

[32] E. Yablonovitch, "Thermodynamics of the fluorescent planar concentrator", J. Opt. Soc. Am. **70**, 1362–1363 (1980).

[33] A. Goetzberger and W. Greube, "Solar energy conversion with fluorescent collectors", Applied physics **14**, 123–139 (1977).

[34] A. Luque and S. Hegedus, *Handbook of photovoltaic science and engineering* (John Wiley & Sons, Led, Chichester, UK, 2010).

[35]B. Richards, "Enhancing the performance of silicon solar cells via the application of passive luminescence conversion layers", Solar Energy Materials and Solar Cells **90**, Selected Papers from the Solar Cells and Solar Energy Materials Symposium -IMRC 2005, 2329–2337 (2006).

[36]E. Klampaftis, D. Ross, K. R. McIntosh, and B. S. Richards, "Enhancing the performance of solar cells via luminescent down-shifting of the incident spectrum: a review", Solar Energy Materials and Solar Cells **93**, 1182–1194 (2009).

[37]F. Meinardi, S. Ehrenberg, L. Dhamo, F. Carulli, M. Mauri, F. Bruni, R. Simonutti, U. Kortshagen, and S. Brovelli, "Highly efficient luminescent solar concentrators based on earth-abundant indirect-bandgap silicon quantum dots", Nature Photonics **11**, 177–185 (2017).

[38]F. Meinardi, H. McDaniel, F. Carulli, A. Colombo, K. A. Velizhanin, N. S. Makarov, R. Simonutti, V. I. Klimov, and S. Brovelli, "Highly efficient large-area colourless luminescent solar concentrators using heavy-metal-free colloidal quantum dots", Nature Nanotechnology **10**, 878–885 (2015).

[39]N. D. Bronstein, Y. Yao, L. Xu, E. O'Brien, A. S. Powers, V. E. Ferry, A. P. Alivisatos, and R. G. Nuzzo, "Quantum dot luminescent concentrator cavity exhibiting 30-fold concentration", ACS Photonics **2**, 1576–1583 (2015).

[40]I. Coropceanu and M. G. Bawendi, "Core/shell quantum dot based luminescent solar concentrators with reduced reabsorption and enhanced efficiency", Nano Letters **14**, 4097–4101 (2014).

[41]L. R. Bradshaw, K. E. Knowles, S. McDowall, and D. R. Gamelin, "Nanocrystals for luminescent solar concentrators", Nano Letters **15**, 1315–1323 (2015).

[42]V. I. Klimov, T. A. Baker, J. Lim, K. A. Velizhanin, and H. McDaniel, "Quality factor of luminescent solar concentrators and practical concentration limits attainable with semiconductor quantum dots", ACS Photonics **3**, 1138–1148 (2016).

[43]I. Papakonstantinou and C. Tummeltshammer, "Fundamental limits of concentration in luminescent solar concentrators revised: the effect of reabsorption and nonunity quantum yield", Optica **2**, 841–849 (2015).

[44]C. B. Murray, C. R. Kagan, and M. G. Bawendi, "Synthesis and characterization of monodisperse nanocrystals and close-packed nanocrystal assemblies", Annual Review of Materials Science **30**, 545–610 (2000).

[45]N. Kholmicheva, P. Moroz, E. Bastola, N. Razgoniaeva, J. Bocanegra, M. Shaughnessy, Z. Porach, D. Khon, and M. Zamkov, "Mapping the exciton diffusion in semiconductor nanocrystal solids", ACS Nano **9**, 2926–2937 (2015).

[46]C. R. Kagan and C. B. Murry, "Charge transport in strongly coupled quantum dot solids", Nat. Nano. **10**, 1013–1026 (2015).

[47]C. R. Kagan, C. B. Murray, and M. G. Bawendi, "Long-range resonance transfer of electronic excitations in close-packed cdse quantum-dot solids", Phys. Rev. B **54**, 8633–8643 (1996).

[48]M. Scheele, J. H. Engel, V. E. Ferry, D. Hanifi, Y. Liu, and A. P. Alivisatos, "Nonmonotonic size dependence in the hole mobility of methoxide-stabilized pbse quantum dot solids", ACS Nano **7**, 6774–6781 (2013).

[49]H. Döllefeld, H. Weller, and A. Eychmüller, "Semiconductor nanocrystal assemblies: experimental pitfalls and a simple model of particle-particle interaction", J. Phys. Chem. B **106**, 5604–5608 (2002).

[50]S. Kühn, U. Håkanson, L. Rogobete, and V. Sandoghdar, "Enhancement of single-molecule fluorescence using a gold nanoparticle as an optical nanoantenna", Phys. Rev. Lett. **97**, 017402 (2006).

[51]K. T. Shimizu, W. K. Woo, B. R. Fisher, H. J. Eisler, and M. G. Bawendi, "Surface-enhanced emission from single semiconductor nanocrystals", Phys. Rev. Lett. **89**, 117401 (2002).

[52]P. Anger, P. Bharadwaj, and L. Novotny, "Enhancement and quenching of single-molecule fluorescence", Phys. Rev. Lett. **96**, 113002 (2006).

[53]V. R. Manfrinato, D. D. Wanger, D. B. Strasfeld, H.-S. Han, F. Marsili, J. P. Arrieta, T. S. Mentzel, M. G. Bawendi, and K. K. Berggren, "Controlled placement of colloidal quantum dots in sub-15 nm clusters", Nanotechnology **24**, 125302 (2013).

[54]G. M. Akselrod, F. Prins, L. V. Poulikakos, E. M. Y. Lee, M. C. Weidman, A. J. Mork, A. P. Willard, V. Bulović, and W. A. Tisdale, "Subdiffusive exciton transport in quantum dot solids", Nano Letters **14**, 3556–3562 (2014).

[55]A. J. Mork, M. C. Weidman, F. Prins, and W. A. Tisdale, "Magnitude of the förster radius in colloidal quantum dot solids", The Journal of Physical Chemistry C **118**, 13920–13928 (2014).

[56]E. M. Y. Lee and W. A. Tisdale, "Determination of exciton diffusion length by transient photoluminescence quenching and its application to quantum dot films", The Journal of Physical Chemistry C **119**, 9005–9015 (2015).

[57] O. Kulakovich, N. Strekal, A. Yaroshevich, S. Maskevich, S. Gaponenko, I. Nabiev, U. Woggon, and M. Artemyev, "Enhanced luminescence of cdse quantum dots on gold colloids", Nano Letters **2**, 1449–1452 (2002).

[58] A. Rakovich, P. Albella, and S. A. Maier, "Plasmonic control of radiative properties of semiconductor quantum dots coupled to plasmonic ring cavities", ACS Nano **9**, 2648–2658 (2015).

[59] M. Nirmal and L. Brus, "Luminescence photophysics in semiconductor nanocrystals", Accounts of Chemical Research, 407–414 (1999).

[60] W. G. J. H. M. van Sark, P. L. T. M. Frederix, A. A. Bol, H. C. Gerritsen, and A. Meijerink, "Blueing, bleaching, and blinking of single cdse/zns quantum dots", ChemPhysChem **3**, 871–879 (2002).

[61] K. T. Shimizu, R. G. Neuhauser, C. A. Leatherdale, S. A. Empedocles, W. K. Woo, and M. G. Bawendi, "Blinking statistics in single semiconductor nanocrystal quantum dots", Phys. Rev. B **63**, 205316 (2001).

[62] Y. J. Na, S. J. Park, S. W. Lee, and J. S. Kim, "Photolithographic process for the patterning of quantum dots", Ultramicroscopy **108**, 1297–1301 (2008).

[63] P. Nordlander, "The ring: a leitmotif in plasmonics", ACS Nano **3**, 488–492 (2009).

[64] J. Aizpurua, P. Hanarp, D. Sutherland, G. Bryant, and J. Garcia de Abajo, "Optical properties of gold nanorings", Physical review letters **90**, 057401 (2003).

[65] H.-M. Gong, L. Zhou, X.-R. Su, S. Xiao, S.-D. Liu, and Q.-Q. Wang, "Illuminating dark plasmons of silver nanoantenna rings to enhance exciton–plasmon interactions", Advanced Functional Materials **19**, 298–303 (2009).

[66]N. Large, J. Aizpurua, V. K. Lin, S. L. Teo, R. Marty, S. Tripathy, and A. Mlayah, "Plasmonic properties of gold ring-disk nano-resonators: fine shape details matter", Opt. Express **19**, 5587–5595 (2011).

[67]S. D. Liu, Z. S. Zhang, and Q. Q. Wang, "High sensitivity and large field enhancement of symmetry broken au nanorings: effect of multipolar plasmon resonance and propagation", Opt. Express **17**, 2906–2917 (2009).

[68]F. Hao, P. Nordlander, M. T. Burnett, and S. A. Maier, "Enhanced tunability and linewidth sharpening of plasmon resonances in hybridized metallic ring/disk nanocavities", Phys. Rev. B **76**, 245417 (2007).

[69]F. Hao, P. Nordlander, Y. Sonnefraud, P. V. Dorpe, and S. A. Maier, "Tunability of subradiant dipolar and fano-type plasmon resonances in metallic ring/disk cavities: implications for nanoscale optical sensing", ACS Nano **3**, 643–652 (2009).

[70]N. Livneh, M. G. Harats, S. Yochelis, Y. Paltiel, and R. Rapaport, "Efficient collection of light from colloidal quantum dots with a hybrid metal–dielectric nanoantenna", ACS Photonics **2**, 1669–1674 (2015).

[71]W. Chen, D. C. Abeysinghe, R. L. Nelson, and Q. Zhan, "Plasmonic lens made of multiple concentric metallic rings under radially polarized illumination", Nano Letters **9**, 4320–4325 (2009).

[72]C. E. Hofmann, E. J. R. Vesseur, L. A. Sweatlock, H. J. Lezec, F. J. García de Abajo, A. Polman, and H. A. Atwater, "Plasmonic modes of annular nanoresonators imaged by spectrally resolved cathodoluminescence", Nano Letters **7**, 3612–3617 (2007).

[73] Y. Gao, L. Y. M. Tobing, A. Kiffer, D. H. Zhang, C. Dang, and H. V. Demir, "Azimuthally polarized, circular colloidal quantum dot laser beam enabled by a concentric grating", ACS Photonics **3**, 2255–2261 (2016).

[74] D. W. de Quilettes, S. M. Vorpahl, S. D. Stranks, H. Nagaoka, G. E. Eperon, M. E. Ziffer, H. J. Snaith, and D. S. Ginger, "Impact of microstructure on local carrier lifetime in perovskite solar cells", Science **348**, 683–686 (2015).

[75] Lumerical, *Fdtd solutions*, `https://www.lumerical.com/products/fdtd/`, 2020.

[76] A. D. Rakić, A. B. Djurišić, J. M. Elazar, and M. L. Majewski, "Optical properties of metallic films for vertical-cavity optoelectronic devices", Applied Optics **37**, 5271–5283 (1998).

[77] Lumerical, *Optoelectronic modeling of photosensitive devices*, `https://www.lumerical.com/support/whitepaper/optoelectronic_modeling_photosensitive_devices.html`, 2020.

[78] A. G. Curto, G. Volpe, T. H. Taminiau, M. P. Kreuzer, R. Quidant, and N. F. van Hulst, "Unidirectional emission of a quantum dot coupled to a nanoantenna", Science **329**, 930–933 (2010).

[79] D. Sehgal and I. K. Vijay, "A method for the high efficiency of water-soluble carbodiimide-mediated amidation", Analytical Biochemistry **218**, 87–91 (1994).

[80] N. Gartmann, C. Schütze, H. Ritter, and D. Brühwiler, "The effect of water on the functionalization of mesoporous silica with 3-aminopropyltriethoxysilane", The Journal of Physical Chemistry Letters **1**, 379–382 (2010).

[81]D. B. Dement, M. K. Quan, and V. E. Ferry, "Nanoscale patterning of colloidal nanocrystal films for nanophotonic applications using direct write electron beam lithography", ACS Applied Materials & Interfaces **11**, 14970–14979 (2019).

[82]A. Ahmed, M. Pelton, and J. R. Guest, "Understanding how acoustic vibrations modulate the optical response of plasmonic metal nanoparticles", ACS Nano **11**, 9360–9369 (2017).

[83]V. Amendola, R. Pilot, M. Frasconi, O. M. Maragò, and M. A. Iatı, "Surface plasmon resonance in gold nanoparticles: a review", Journal of Physics: Condensed Matter **29**, 203002 (2017).

[84]S. Link and M. A. El-Sayed, "Optical properties and ultrafast dynamics of metallic nanocrystals", Annual Review of Physical Chemistry **54**, 331–366 (2003).

[85]H. Baida, D. Mongin, D. Christofilos, G. Bachelier, A. Crut, P. Maioli, N. Del Fatti, and F. Vallée, "Ultrafast nonlinear optical response of a single gold nanorod near its surface plasmon resonance", Phys. Rev. Lett. **107**, 057402 (2011).

[86]M. Perner, P. Bost, U. Lemmer, G. von Plessen, J. Feldmann, U. Becker, M. Mennig, M. Schmitt, and H. Schmidt, "Optically induced damping of the surface plasmon resonance in gold colloids", Phys. Rev. Lett. **78**, 2192–2195 (1997).

[87]C. Voisin, N. Del Fatti, D. Christofilos, and F. Vallée, "Ultrafast electron dynamics and optical nonlinearities in metal nanoparticles", The Journal of Physical Chemistry B **105**, 2264–2280 (2001).

[88]J. R. M. Saavedra, A. Asenjo-Garcia, and F. J. García de Abajo, "Hot-electron dynamics and thermalization in small metallic nanoparticles", ACS Photonics **3**, 1637–1646 (2016).

[89]S. Link and M. A. El-Sayed, "Size and temperature dependence of the plasmon absorption of colloidal gold nanoparticles", The Journal of Physical Chemistry B **103**, 4212–4217 (1999).

[90]F. Medeghini, R. Rouxel, A. Crut, P. Maioli, F. Rossella, F. Banfi, F. Vallée, and N. Del Fatti, "Signatures of small morphological anisotropies in the plasmonic and vibrational responses of individual nano-objects", The Journal of Physical Chemistry Letters **10**, 5372–5380 (2019).

[91]M. Pelton, M. Liu, S. Park, N. Scherer, and P. Guyot-Sionnest, "Ultrafast resonant optical scattering from single gold nanorods: large nonlinearities and plasmon saturation", English, Physical Review B-Condensed Matter **73** (2006).

[92]J. Olson, S. Dominguez-Medina, A. Hoggard, L.-Y. Wang, W.-S. Chang, and S. Link, "Optical characterization of single plasmonic nanoparticles", Chem. Soc. Rev. **44**, 40–57 (2015).

[93]G. Beane, T. Devkota, B. S. Brown, and G. V. Hartland, "Ultrafast measurements of the dynamics of single nanostructures: a review", Reports on Progress in Physics **82**, 016401 (2018).

[94]W.-S. Chang, F. Wen, D. Chakraborty, M.-N. Su, Y. Zhang, B. Shuang, P. Nordlander, J. E. Sader, N. J. Halas, and S. Link, "Tuning the acoustic frequency of a gold nanodisk through its adhesion layer", Nature Communications **6**, 7022 (2015).

[95]M. ElKabbash, A. R. Rashed, B. Kucukoz, Q. Nguyen, A. Karatay, G. Yaglioglu, E. Ozbay, H. Caglayan, and G. Strangi, "Ultrafast transient optical loss dynamics in exciton–plasmon nano-assemblies", Nanoscale **9**, 6558–6566 (2017).

[96]W. Wang, P. Vasa, R. Pomraenke, R. Vogelgesang, A. De Sio, E. Sommer, M. Maiuri, C. Manzoni, G. Cerullo, and C. Lienau, "Interplay between strong coupling and radiative damping of excitons and surface plasmon polaritons in hybrid nanostructures", ACS Nano **8**, 1056–1064 (2014).

[97]J. N. Clark, L. Beitra, G. Xiong, A. Higginbotham, D. M. Fritz, H. T. Lemke, D. Zhu, M. Chollet, G. J. Williams, M. Messerschmidt, B. Abbey, R. J. Harder, A. M. Korsunsky, J. S. Wark, and I. K. Robinson, "Ultrafast three-dimensional imaging of lattice dynamics in individual gold nanocrystals", Science **341**, 56–59 (2013).

[98]D. T. Valley, V. E. Ferry, and D. J. Flannigan, "Imaging intra- and interparticle acousto-plasmonic vibrational dynamics with ultrafast electron microscopy", Nano Letters **16**, 7302–7308 (2016).

[99]Y.-J. Kim, H. Jung, S. W. Han, and O.-H. Kwon, "Ultrafast electron microscopy visualizes acoustic vibrations of plasmonic nanorods at the interfaces", Matter **1**, 481–495 (2019).

[100]S. Link, C. Burda, M. B. Mohamed, B. Nikoobakht, and M. A. El-Sayed, "Femtosecond transient-absorption dynamics of colloidal gold nanorods: shape independence of the electron-phonon relaxation time", Phys. Rev. B **61**, 6086–6090 (2000).

[101]G. V. Hartland, "Optical studies of dynamics in noble metal nanostructures", Chemical Reviews **111**, 3858–3887 (2011).

[102]A. Crut, P. Maioli, N. Del Fatti, and F. Vallée, "Acoustic vibrations of metal nano-objects: time-domain investigations", Physics Reports **549**, Acoustic vibrations of metal nano-objects: Time-domain investigations, 1–43 (2015).

[103]B. Rethfeld, A. Kaiser, M. Vicanek, and G. Simon, "Nonequilibrium electron and phonon dynamics in solids absorbing a subpicosecond laser pulse", in Nonresonant laser-matter interaction (nlmi-10), Vol. 4423, edited by M. N. Libenson (International Society for Optics and Photonics, 2001), pp. 250–261.

[104]J. R. M. Saavedra, A. Asenjo-Garcia, and F. J. García de Abajo, "Hot-electron dynamics and thermalization in small metallic nanoparticles", ACS Photonics **3**, 1637–1646 (2016).

[105]P. V. Ruijgrok, P. Zijlstra, A. L. Tchebotareva, and M. Orrit, "Damping of acoustic vibrations of single gold nanoparticles optically trapped in water", Nano Letters **12**, 1063–1069 (2012).

[106]T. A. Major, S. S. Lo, K. Yu, and G. V. Hartland, "Time-resolved studies of the acoustic vibrational modes of metal and semiconductor nano-objects", The Journal of Physical Chemistry Letters **5**, 866–874 (2014).

[107]M. A. Mahmoud, D. O'Neil, and M. A. El-Sayed, "Shape- and symmetry-dependent mechanical properties of metallic gold and silver on the nanoscale", Nano Letters **14**, 743–748 (2014).

[108]T. A. Kelf, Y. Tanaka, O. Matsuda, E. M. Larsson, D. S. Sutherland, and O. B. Wright, "Ultrafast vibrations of gold nanorings", Nano Letters **11**, 3893–3898 (2011).

[109]Y.-H. Qiu, F. Nan, Y.-F. Zhang, J.-H. Wang, G.-Y. He, L. Zhou, and Q.-Q. Wang, "Size-dependent plasmon relaxation dynamics and saturable absorption in gold nanorods", Journal of Physics D: Applied Physics **49**, 185107 (2016).

[110]B. Rethfeld, A. Kaiser, M. Vicanek, and G. Simon, "Nonequilibrium electron and phonon dynamics in solids absorbing a subpicosecond laser pulse", in Nonresonant laser-matter interaction (nlmi-10), Vol. 4423, edited by M. N. Libenson (International Society for Optics and Photonics, 2001), pp. 250–261.

[111]B. Rethfeld, A. Kaiser, M. Vicanek, and G. Simon, "Ultrafast dynamics of nonequilibrium electrons in metals under femtosecond laser irradiation", Phys. Rev. B **65**, 214303 (2002).

[112]G. Kedawat, I. Sharma, K. Nagpal, M. Kumar, G. Gupta, and B. K. Gupta, "Studies of ultrafast transient absorption spectroscopy of gold nanorods in an aqueous solution", ACS Omega **4**, 12626–12631 (2019).

[113]A. Ahmed, M. Pelton, and J. R. Guest, "Understanding how acoustic vibrations modulate the optical response of plasmonic metal nanoparticles", ACS Nano **11**, 9360–9369 (2017).

[114]G. Wehmeyer, K. C. Bustillo, A. M. Minor, and C. Dames, "Measuring temperature-dependent thermal diffuse scattering using scanning transmission electron microscopy", Applied Physics Letters **113**, 253101 (2018).

[115]L. He and R. Hull, "Quantification of electron–phonon scattering for determination of temperature variations at high spatial resolution in the transmission electron microscope", Nanotechnology **23**, 205705 (2012).

[116]C. R. Hall and P. B. Hirsch, "Effect of thermal diffuse scattering on propagation of high energy electrons through crystals", Proceedings of the Royal Society of London. Series A. Mathematical and Physical Sciences **286**, 158–177 (1965).

[117] P. Zijlstra, A. L. Tchebotareva, J. W. M. Chon, M. Gu, and M. Orrit, "Acoustic oscillations and elastic moduli of single gold nanorods", Nano Letters **8**, 3493–3497 (2008).

[118] "Crc handbook of chemistry and physics", (1977).

[119] M. Hu, X. Wang, G. V. Hartland, P. Mulvaney, J. P. Juste, and J. E. Sader, "Vibrational response of nanorods to ultrafast laser induced heating: theoretical and experimental analysis", Journal of the American Chemical Society **125**, 14925–14933 (2003).

[120] J. C. Goldschmidt and S. Fischer, "Upconversion for photovoltaics – a review of materials, devices and concepts for performance enhancement", Advanced Optical Materials **3**, 510–535 (2015).

[121] T. Trupke, M. A. Green, and P. Würfel, "Improving solar cell efficiencies by up-conversion of sub-band-gap light", Journal of Applied Physics **92**, 4117–4122 (2002).

[122] Y. Shang, S. Hao, C. Yang, and G. Chen, "Enhancing solar cell efficiency using photon upconversion materials", Nanomaterials (Basel) **5**, 1782–1809 (2015).

[123] A. Monguzzi, R. Tubino, S. Hoseinkhani, M. Campione, and F. Meinardi, "Low power, non-coherent sensitized photon up-conversion: modelling and perspectives", Physical chemistry chemical physics : PCCP **14**, 4322–32 (2012).

[124] A. Monguzzi, D. Braga, M. Gandini, V. C. Holmberg, D. K. Kim, A. Sahu, D. J. Norris, and F. Meinardi, "Broadband up-conversion at subsolar irradiance: triplet–triplet annihilation boosted by fluorescent semiconductor nanocrystals", Nano Letters **14**, 6644–6650 (2014).

[125]N. Yanai and N. Kimizuka, "New triplet sensitization routes for photon upconversion: thermally activated delayed fluorescence molecules, inorganic nanocrystals, and singlet-to-triplet absorption", Accounts of Chemical Research **50**, 2487–2495 (2017).

[126]T. N. Singh-Rachford and F. N. Castellano, "Photon upconversion based on sensitized triplet–triplet annihilation", Coordination Chemistry Reviews **254**, 18th International Symposium on the Photochemistry and Photophysics of Coordination Compounds Sapporo, 2009, 2560–2573 (2010).

[127]B. Joarder, N. Yanai, and N. Kimizuka, "Solid-state photon upconversion materials: structural integrity and triplet–singlet dual energy migration", The Journal of Physical Chemistry Letters **9**, 4613–4624 (2018).

[128]P. Bharmoria, S. Hisamitsu, H. Nagatomi, T. Ogawa, M.-a. Morikawa, N. Yanai, and N. Kimizuka, "Simple and versatile platform for air-tolerant photon upconverting hydrogels by biopolymer–surfactant–chromophore co-assembly", Journal of the American Chemical Society **140**, 10848–10855 (2018).

[129]Y. C. Simon and C. Weder, "Low-power photon upconversion through triplet–triplet annihilation in polymers", J. Mater. Chem. **22**, 20817–20830 (2012).

[130]S. Baluschev, T. Miteva, V. Yakutkin, G. Nelles, A. Yasuda, and G. Wegner, "Upconversion fluorescence: noncoherent excitation by sunlight", Phys. Rev. Lett. **97**, 143903 (2006).

[131]J. Zhou, Q. Liu, W. Feng, Y. Sun, and F. Li, "Upconversion luminescent materials: advances and applications", Chemical Reviews **115**, 395–465 (2015).

[132]V. Yakutkin, S. Aleshchenkov, S. Chernov, T. Miteva, G. Nelles, A. Cheprakov, and S. Baluschev, "Towards the ir limit of the triplet–triplet annihilation-supported up-conversion: tetraanthraporphyrin", Chemistry – A European Journal **14**, 9846–9850 (2008).

[133]S. K. Sugunan, U. Tripathy, S. M. K. Brunet, M. F. Paige, and R. P. Steer, "Mechanisms of low-power noncoherent photon upconversion in metalloporphyrinorganic blue emitter systems in solution", The Journal of Physical Chemistry A **113**, 8548–8556 (2009).

[134]K. Tanaka, K. Inafuku, and Y. Chujo, "Environment-responsive upconversion based on dendrimer-supported efficient triplet–triplet annihilation in aqueous media", Chem. Commun. **46**, 4378–4380 (2010).

[135]A. Monguzzi, M. Frigoli, C. Larpent, R. Tubino, and F. Meinardi, "Low-power-photon up-conversion in dual-dye-loaded polymer nanoparticles", Advanced Functional Materials **22**, 139–143 (2012).

[136]O. S. Kwon, H. S. Song, J. Conde, H.-i. Kim, N. Artzi, and J.-H. Kim, "Dual-color emissive upconversion nanocapsules for differential cancer bioimaging in vivo", ACS Nano **10**, 1512–1521 (2016).

[137]J.-H. Kim and J.-H. Kim, "Encapsulated triplet–triplet annihilation-based upconversion in the aqueous phase for sub-band-gap semiconductor photocatalysis", Journal of the American Chemical Society **134**, 17478–17481 (2012).

[138]D. M. Wu, A. García-Etxarri, A. Salleo, and J. A. Dionne, "Plasmon-enhanced upconversion", The Journal of Physical Chemistry Letters **5**, 4020–4031 (2014).

[139] J. C. Goldschmidt, P. Loper, S. Fischer, S. Janz, M. Peters, S. W. Glunz, G. Willeke, E. Lifshitz, K. Kramer, and D. Biner, "Advanced upconverter systems with spectral and geometric concentration for high upconversion efficiencies", in 2008 conference on optoelectronic and microelectronic materials and devices (2008), pp. 307–311.

[140] M. Wu, D. N. Congreve, M. W. B. Wilson, J. Jean, N. Geva, M. Welborn, T. Van Voorhis, V. Bulović, M. G. Bawendi, and M. A. Baldo, "Solid-state infrared-to-visible upconversion sensitized by colloidal nanocrystals", Nature Photonics **10**, 31–34 (2016).

[141] A. Monguzzi, D. Braga, M. Gandini, V. C. Holmberg, D. K. Kim, A. Sahu, D. J. Norris, and F. Meinardi, "Broadband up-conversion at subsolar irradiance: triplet–triplet annihilation boosted by fluorescent semiconductor nanocrystals", Nano Letters **14**, 6644–6650 (2014).

[142] C. Struempel, M. McCann, C. Cañizo, I. Tobias, and P. Fath, "Erbium-doped up-converters of silicon solar cells: assessment of the potential", Proceedings of the 20th European Photovoltaic Solar Energy Conference, 43–46 (2005).

[143] R. W. Olson, R. F. Loring, and M. D. Fayer, "Luminescent solar concentrators and the reabsorption problem", Appl. Opt. **20**, 2934–2940 (1981).

[144] Z. Krumer, S. J. Pera, R. J. van Dijk-Moes, Y. Zhao, A. F. de Brouwer, E. Groeneveld, W. G. van Sark, R. E. Schropp, and C. de Mello Donegá, "Tackling self-absorption in luminescent solar concentrators with type-ii colloidal quantum dots", Solar Energy Materials and Solar Cells **111**, 57–65 (2013).

[145]J. Bomm, A. Büchtemann, A. J. Chatten, R. Bose, D. J. Farrell, N. L. Chan, Y. Xiao, L. H. Slooff, T. Meyer, A. Meyer, W. G. van Sark, and R. Koole, "Fabrication and full characterization of state-of-the-art quantum dot luminescent solar concentrators", Solar Energy Materials and Solar Cells **95**, Photovoltaics, Solar Energy Materials Thin Films, IMRC 2009-Cancun, 2087–2094 (2011).

[146]I. Papakonstantinou and C. Tummeltshammer, "Fundamental limits of concentration in luminescent solar concentrators revised: the effect of reabsorption and nonunity quantum yield", Optica **2**, 841–849 (2015).

[147]V. Sholin, J. D. Olson, and S. A. Carter, "Semiconducting polymers and quantum dots in luminescent solar concentrators for solar energy harvesting", Journal of Applied Physics **101**, 123114 (2007).

[148]S. Calixto, N. Ganzherli, S. Gulyaev, and S. Figueroa-Gerstenmaier, "Gelatin as a photosensitive material", Molecules **23**, 2064 (2018).

[149]A. Monguzzi, J. Mezyk, F. Scotognella, R. Tubino, and F. Meinardi, "Upconversion-induced fluorescence in multicomponent systems: steady-state excitation power threshold", Phys. Rev. B **78**, 195112 (2008).

[150]A. Bansal, W. Holzer, A. Penzkofer, and T. Tsuboi, "Absorption and emission spectroscopic characterization of platinum-octaethyl-porphyrin (ptoep)", Chemical Physics **330**, 118–129 (2006).

[151]Y. Fujiwara, R. Ozawa, D. Onuma, K. Suzuki, K. Yoza, and K. Kobayashi, "Double alkylene-strapped diphenylanthracene as a photostable and intense solid-state blue-emitting material", The Journal of Organic Chemistry **78**, 2206–2212 (2013).

[152]M. R. Bergren, N. S. Makarov, K. Ramasamy, A. Jackson, R. Guglielmetti, and H. McDaniel, "High-performance cuins2 quantum dot laminated glass luminescent solar concentrators for windows", ACS Energy Letters **3**, 520–525 (2018).

[153]H. Li, K. Wu, J. Lim, H.-J. Song, and V. I. Klimov, "Doctor-blade deposition of quantum dots onto standard window glass for low-loss large-area luminescent solar concentrators", Nature Energy **1**, 16157 (2016).

[154]Y. Cai, Y. Li, P. Nordlander, and P. S. Cremer, "Fabrication of elliptical nanorings with highly tunable and multiple plasmonic resonances", Nano Letters **12**, 4881–4888 (2012).